



National Library
of Canada

Bibliothèque nationale
du Canada

Canadian Theses Service

Service des thèses canadiennes

Ottawa, Canada
K1A 0N4

NOTICE

The quality of this microform is heavily dependent upon the quality of the original thesis submitted for microfilming. Every effort has been made to ensure the highest quality of reproduction possible.

If pages are missing, contact the university which granted the degree.

Some pages may have indistinct print especially if the original pages were typed with a poor typewriter ribbon or if the university sent us an inferior photocopy.

Reproduction in full or in part of this microform is governed by the Canadian Copyright Act, R.S.C. 1970, c. C-30, and subsequent amendments.

AVIS

La qualité de cette microforme dépend grandement de la qualité de la thèse soumise au microfilmage. Nous avons tout fait pour assurer une qualité supérieure de reproduction.

S'il manque des pages, veuillez communiquer avec l'université qui a conféré le grade.

La qualité d'impression de certaines pages peut laisser à désirer, surtout si les pages originales ont été dactylographiées à l'aide d'un ruban usé ou si l'université nous a fait parvenir une photocopie de qualité inférieure.

La reproduction, même partielle, de cette microforme est soumise à la Loi canadienne sur le droit d'auteur, SRC 1970, c. C-30, et ses amendements subséquents.

UNIVERSITY OF ALBERTA

AURORAL ARCS MODULATED BY RESONANT ALFVÉN WAVES

BY



BAOLIAN XU

A THESIS

SUBMITTED TO THE FACULTY OF GRADUATE STUDIES AND RESEARCH

IN PARTIAL FULFILMENT OF THE REQUIREMENTS FOR THE DEGREE

OF

MASTER OF SCIENCE

IN

PHYSICS

DEPARTMENT OF PHYSICS

EDMONTON, ALBERTA

SPRING 1992



National Library
of Canada

Bibliothèque nationale
du Canada

Canadian Theses Service Service des thèses canadiennes

Ottawa, Canada
K1A 0N4

The author has granted an irrevocable non-exclusive licence allowing the National Library of Canada to reproduce, loan, distribute or sell copies of his/her thesis by any means and in any form or format, making this thesis available to interested persons.

The author retains ownership of the copyright in his/her thesis. Neither the thesis nor substantial extracts from it may be printed or otherwise reproduced without his/her permission.

L'auteur a accordé une licence irrévocable et non exclusive permettant à la Bibliothèque nationale du Canada de reproduire, prêter, distribuer ou vendre des copies de sa thèse de quelque manière et sous quelque forme que ce soit pour mettre des exemplaires de cette thèse à la disposition des personnes intéressées.

L'auteur conserve la propriété du droit d'auteur qui protège sa thèse. Ni la thèse ni des extraits substantiels de celle-ci ne doivent être imprimés ou autrement reproduits sans son autorisation.

ISBN 0-315-73112-5

Canada

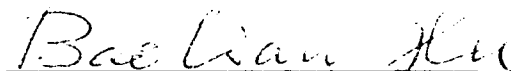
UNIVERSITY OF ALBERTA

RELEASE FORM

NAME OF AUTHOR Baolian Xu
TITLE OF THESIS Auroral Arcs Modulated by Resonant Alfvén Waves
DEGREE Master of Science
YEAR THIS DEGREE GRANTED 1992

Permission is hereby granted to UNIVERSITY OF ALBERTA LIBRARY to reproduce single copies of this thesis and to lend or sell such copies for private, scholarly or scientific research purposes only.

The author reserves other publication rights, and neither the thesis nor extensive extracts from it may be printed or otherwise reproduced without the author's written permission.



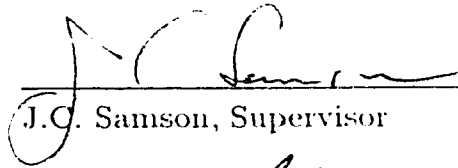
Baolian Xu
Department of Physics
University of Alberta
Edmonton, Alberta
T6G 2J1

Date: December 3, 1991


UNIVERSITY OF ALBERTA

FACULTY OF GRADUATE STUDIES AND RESEARCH

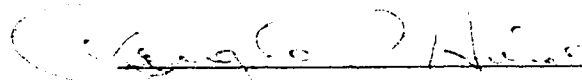
The undersigned certify that they have read, and recommend to the Faculty of Graduate Studies and Research for acceptance, a thesis entitled "Auroral Arcs Modulated by Resonant Alfvén Waves" submitted by Baolian Xu in partial fulfilment of the requirements for the degree of Master of Science in Physics.



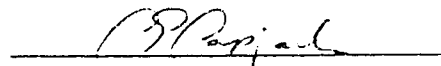
J.C. Samson, Supervisor



G. Rostoker



D.P. Húbe



C.E. Capjack

Date: December 3, 1991

ABSTRACT

Optical aurora and resonant Alfvén waves in the magnetosphere share a number of common features. In our observations of optical 5577 Å, 6300 Å and 4861 Å emissions and magnetic disturbances on the ground, we find sufficient evidence to prove that the resonant Alfvén waves or field line resonances strongly modulate the luminosity of pre-substorm auroral arcs. The fundamental frequency is about 1.1 - 1.4 *mHz*. The latitudinal phase change of 6300 Å emission caused by the low-energy electron precipitation has a local minimum corresponding to the position of the maximum power in the power spectrum.

On the basis of the MHD theory, a tunnel coupling model is set up to compare the modulation relation between the resonant Alfvén waves and electron precipitation on the macroscopic scale of the electric field. By analyzing the observational evidence and theoretical result, we conclude that there is a resonant width in the resonant Alfvén wave field defined by the distance between the resonant and turning points, and the modulation of the electron precipitation occurs in this region. The local minimum of latitudinal phase change is due to the energy reflection of the waves by the turning point in the magnetosphere.

ACKNOWLEDGEMENTS

I wish to express thanks to Dr. J. C. Samson who supervised this project. I also express thanks to Dr. G. Rostoker who has given helpful suggestions during the course of the research. Special thanks are due to Dr. T. Hughes and Dr. F. Creutzberg who collaborated in the project. They provided hospitable receptions when I spent a short period studying in the Herzberg Institute of Astrophysics, National Research Council of Canada in Ottawa. Thanks are also due to Mrs. K. Apps, Mrs. B. Tooley, Mr. M. Connors and Mr. S. Botsford. They gave me great helps in computational and other daily routines. I would like to appreciate Dr. W. W. Liu and Dr. B. Harrold for their helpful discussions and comments on the thesis. I wish to thank Mr. Q. Liu for providing the word processing software for type setting this thesis.

I finally express special thanks for my wife, Wenjun Bie and son, David Shou. Their patience, understanding, encouragement and support ensured the successful conclusions of the project.

TABLE OF CONTENTS

1	INTRODUCTION	1
1.1	The auroral oval and discrete arc formation	1
1.2	Field line oscillations and resonant Alfvén waves	3
1.3	Kinetic Alfvén waves and auroral particle precipitation	4
1.4	Purpose of the project	5
2	THE THEORY OF ULF MHD WAVES IN THE MAGNETOSPHERE	7
2.1	MHD equations in a nonuniform plasma	7
2.2	MHD waves in the magnetosphere	11
2.2.1	Southwood-Chen-Hasegawa theoretical model	11
2.2.2	Global models	12
2.3	WKB solutions in nonuniform plasma	13
2.4	Numerical solutions for the coupled model with tunnelling	16
2.4.1	The complex solution of the differential equation	16
2.4.2	Resonant absorption and energy absorption rate	19
2.5	Kinetic Alfvén waves and auroral electrons	20
3	INSTRUMENTATION AND METHODS	29
3.1	CANOPUS — the data campaign in our project	29
3.1.1	Meridian Photometer Array (MPA)	29

3.1.2	Magnetometer and Riometer Array (MARIA)	30
3.2	Objectives and method	31
3.2.1	Parameters observed in the project	31
3.2.2	Auroral emissions and MPA data	32
3.2.3	The method of data processing	33
4	OBSERVATIONS OF AURORAL ARCS AND ASSOCIATED RESONANT ALFVÉN WAVES	38
4.1	Observations of ULF waves in the magnetometer data	38
4.2	Observations of MPA aurora	39
4.3	Data analysis	40
4.3.1	Event 88272, 3:00-4:00 UT	40
4.3.2	Event 89342, 5:00-6:00 UT	41
4.3.3	Event 89343, 4:00-5:00 UT	42
5	DISCUSSION AND CONCLUSIONS	66
5.1	The resonance seen in the magnetometer data	66
5.2	The resonance seen in phase shift in the MPA aurora	67
5.3	Modulated optical arcs and inverted V	68
5.4	Conclusions	69
	APPENDICES	73
A	BUDDEN'S COMPUTATIONAL METHOD	73

B	COMPLEX DEMODULATION METHOD	75
	BIBLIOGRAPHY	78

LIST OF TABLES

3.1	Latitude conversion table for MPA data	35
3.2	Location of magnetometer stations	36

LIST OF FIGURES

2.1	Schematic representation for tunnel coupling model in the flank region of the magnetosphere	23
2.2	The energy absorption coefficient in the resonant Alfvén wave region	24
2.3	Numerical solutions for Y_1	25
2.4	Numerical solutions for Y_2	26
2.5	Numerical solutions for Y_3	27
2.6	Phases of normalized Y_1 , Y_2 and Y_3	28
3.1	CANOPUS system map	37
4.1	X-component of magnetometer data recorded by the eastern line of the CANOPUS system on September 28, 1988	44
4.2	X-component of magnetometer data recorded by the eastern line of the CANOPUS system on December 8, 1989	45
4.3	X-component of magnetometer data recorded by the eastern line of the CANOPUS system on December 9, 1989	46
4.4	Auroral intensity of MPA data against time and Invariant latitude for event 88272 at Gillam	47
4.5	Auroral intensity of MPA data against time and Invariant latitude for event 89342 at Gillam	48
4.6	Auroral intensity of MPA data against time and Invariant latitude for event 89342 at Rankin Inlet	49

4.7	Auroral intensity of MPA data against time and Invariant latitude for event 89343 at Rankin Inlet	50
4.8	Example: Comparison of modulated emission intensity with original total emission intensity in optical aurora.	51
4.9	Pure state power spectrum for the X+Y+Z components and ellipticity on the X-Y plane in the interval from 3:00 to 4:00 UT, on September 28, 1988	52
4.10	Pure state power and ellipticity for 4 stations for event 88272	53
4.11	Power spectra of MPA 5577 Å emissions observed at Gillam station for event 88272	54
4.12	Power spectra of MPA 6300 Å emissions observed at Gillam station for event 88272	55
4.13	The contour plot of MPA power and phase of the 5577 Å emissions for event 88272 at Gillam station	56
4.14	The contour plot of MPA power and phase of the 6300 Å emissions for event 88272 at Gillam station	57
4.15	Pure state power spectrum for the X+Y+Z components and ellipticity on the X-Y plane in the interval from 5:00 to 6:00 UT, on December 8, 1989	58
4.16	Pure state power and ellipticity for 6 stations for event 89342	59
4.17	MPA power and phase of the 5577 Å and 6300 Å emissions for event 89342 at Gillam station	60

4.18	Pure state power spectrum for the X+Y+Z components and ellipticity on the X-Y plane in the interval from 4:00 to 5:00 UT, on December 9, 1989	61
4.19	Pure state power and ellipticity for 6 stations for event 89343 . . .	62
4.20	The contour plot of MPA power and phase of the 5577 Å emissions for event 89343 at Rankin station	63
4.21	The contour plot of MPA power and phase of the 6300 Å emissions for event 89343 at Rankin station	64
4.22	The contour plot of MPA power and phase of the 6300 Å emissions for event 89343 at Gillam station	65
5.1	The polarization ratio ξ_x/ξ_y . Y_2 and Y_3 are normalized ξ_x and ξ_y defined in Chapter 2.	71
5.2	Top: (a) Schematic representation for resonant magnetometer data. Bottom: (b) Schematic representation for modulated MPA data. .	72
A.1	ζ complex plane analysis of WKB asymptotic solution	74
B.1	Schematic diagram of the procedure for computing the complex demodulation method.	77

Chapter One

INTRODUCTION

Ultra-low-frequency (ULF) magnetohydrodynamic (MHD) waves are important energy carriers in the process leading to the coupling of the magnetosphere and ionosphere (Goertz, 1979). These waves transport considerable energy from the magnetosphere into the ionosphere. During this energy transmission process, wave-particle interactions often play an important role, producing energetic electrons leading to the auroral displays seen at high latitudes. One possible mechanism giving particle precipitation into the auroral region is connected with resonant Alfvén waves on magnetic field lines threading the auroral oval (Samson, 1991a; 1991c). These Alfvén resonances and discrete arcs have many similar features. The first purpose of this project is to examine observational evidence in the ground based optical photometer data and magnetometer data to determine the possible connections between the MHD field line resonance and auroral particle precipitation. The second is to set up a macroscopic, theoretical model using MHD wave equations to explain the relation between auroral arcs and resonant Alfvén waves.

1.1 The auroral oval and discrete arc formation

The active auroral region occurring in the Earth's ionosphere is called the auroral oval. The latitudinal location of the oval coincides with the maximum intensity of ULF magnetic field line oscillations or pulsations (Samson, 1972; Saito, 1969). In our research we shall restrict our study to the night side auroral zone, in the pre-midnight sector.

According to the classification in the International Auroral Atlas (1963), an auroral arc appears as a slightly curving arch or part of an arch in the auroral ionosphere. Stable arcs are seldom very bright and have thin curtain-like forms, often with multiple curtains (Akasofu, 1981). Most arcs are due to electron precipitation, but precipitation of energetic hydrogen ions can also give auroral emissions, particularly at 4861 \AA H_{β} and 5577 \AA . These proton arcs tend to be much broader (typically greater than $1 - 2^{\circ}$ latitude) and are usually subvisual.

Electron aurora can have very small scale size due to the small gyro-radii of electron orbits in the magnetic field. The approximate gyroradius of a 10 keV electron in the Earth's magnetic field in the auroral zone is only about 6 m or less (Omholt, 1971). The scale size of the electron aurora in the north-south direction ranges from a fraction of a km to about 100 km. Using magnetic flux conservation, we can approximate the dimension of a discrete electron auroral arc in the magnetosphere. A hundred kilometer wide arc at 70° Invariant latitude maps to a radial scale size of 1 R_E (Earth's radius) in the equatorial plane of the magnetosphere. The height of the lower edge of an auroral arc in the upper atmosphere is typically 100 km, and its upper edge is at about 400 km or more.

Compared with the electron aurora, proton aurorae have large north-south scale sizes due to the large gyroradius of the proton and collisions in the ionosphere. The proton gyroradius is 50 times larger than the electron's gyroradius if it has the same energy as the electron (Omholt, 1971). Some studies have found that, in the evening sector, proton aurorae generally occur equatorward of the stronger, distinct electron aurora (Rees and Benedict, 1970), and closer to the electron aurora in the morning hours than at midnight (Wiens and Vallance Jones, 1969).

In our project, we are interested in the discrete arcs which might be associated with the resonant Alfvén waves. These arcs usually have about 100's to

several thousand Rayleigh (kR) of green 5577 \AA optical emissions and are produced by electrons with energies typically greater than 1 keV (Rees, 1974). At the same time, the red line 6300 \AA often has a much lower optical intensity, usually less than 1 kR. This line is produced by low energy electrons (typical energies are 100's of eV). If H_{β} (4861 \AA) occurs, and the 5577 \AA line has intensities of several hundreds R, then the emissions may be produced by energetic protons (10's of keV or greater).

1.2 Field line oscillations and resonant Alfvén waves

The solutions of the linearized MHD equations indicate that there is a coupling between the compressional and shear Alfvén waves at the position of the resonance (Kivelson and Southwood, 1985; Kivelson, 1986; Allan, 1986). There is now sufficient experimental evidence to confirm the existence of these resonances in the Earth's magnetosphere (Samson, 1991b).

Numerous articles have been published on the topic of MHD coupling. Dungey (1954) first developed the wave equations which are appropriate for a dipole field geometry. The equations for the two transverse magnetic field components are coupled except in a limited number of special cases. If we assume that the azimuthal or longitudinal dependence is given by $e^{im\Phi}$, then for $m = 0$, the azimuthal and poloidal components are uncoupled. Tamao (1966) used the coupled set of equations for a dipole system, but looked for solutions valid near the equator. He found that a region of resonant coupling would occur, where the amplitudes of the magnetic field oscillations have singularities.

A somewhat more comprehensive model of MHD resonances including the Kelvin-Helmholtz instability as a source of energy at the magnetopause, was set up by Southwood (1974), and Chen and Hasegawa (1974a). Chen and Hasegawa also limited their solution to regions near the equatorial plane. Both Southwood's and

Chen and Hasegawa's models can successfully explain the variation of amplitude with latitude and the associated latitudinal variation of the polarization of the waves (Samson, 1972).

In order to produce the quantized spectra of MHD waves and resonances, Kivelson and Southwood (1985, 1986) proposed a global MHD coupling model. This model is not restricted to the large m limit and has the form of global compressional eigenmodes, whose frequencies are quantized by the radial structure of the magnetosphere and by the azimuthal wave number. For $m = 0$, a global compressional wave is established. For $m \neq 0$, the wave modes are damped through irreversible coupling to an Alfvén mode localized to magnetic field line with the same resonant frequency. Numerical and computational models have been used to study the various theoretical ideas with different geometries for the cavity modes (Allan ,1986; Zhu and Kivelson , 1988). All the above studies show that compressional energy is absorbed by shear Alfvén waves at the resonance position, leading to resonant vibrations of the field lines.

1.3 Kinetic Alfvén waves and auroral particle precipitation

The theoretical work we have discussed above did not consider the effects of particles on the evolution of the MHD waves. In fact, the shear Alfvén wave is dispersive if $k_{\perp} \neq 0$, *i.e.*, if it does not exactly propagate along the background magnetic field. Hasegawa (1975, 1976) called this kind of shear Alfvén wave, with a finite perpendicular wavelength (ρ_{\perp}), the kinetic Alfvén wave. These waves have longer wavelengths in the direction parallel to the magnetic field, and a scale length comparable to the ion gyroradius ($\sim \rho_i$) in the perpendicular direction. An important property of the kinetic Alfvén wave is the existence of a parallel electric field in the wave. This parallel electric field can cause charged particle

acceleration and precipitation into the ionosphere.

The kinetic processes in mode conversion to the kinetic Alfvén waves have been considered by a number of authors (Hasegawa and Chen, 1975; Hasegawa, 1976; Hasegawa and Mima, 1978; Goertz, 1979, 1984; Hasegawa and MacLennan, 1990). They suggest that plasma heating occurs when the kinetic Alfvén wave is dissipated by wave-particle interactions (Landau damping). The process of plasma heating in microscopic space is much like a particle phase mixing process (Hasegawa, 1976). In Hasegawa's scenario, the surface wave on a plasma discontinuity in the magnetosphere is mode converted to a kinetic Alfvén wave. The kinetic Alfvén wave has a field-aligned electric field that oscillates at the same frequency as the surface wave. In Hasegawa's model, the auroral electrons are accelerated by the parallel electric field, leading to the formation of a discrete auroral arc.

Goertz (1981) separated the auroral arcs associated with the kinetic Alfvén wave effects into two kinds, depending upon their k_{\perp} . The large k_{\perp} components dissipate their energy by rapidly accelerating electrons. They give the strong acceleration which occurs in narrow auroral arc structures. However, the small k_{\perp} components do not suffer significant dispersive damping. They will survive many wave bounce periods, eventually establishing a standing wave pattern. This kind of arc has a somewhat larger time and spatial scale that can expand to a few hundred km in the north-south direction. It may be associated with inverted V arc formation. Using this analysis, Goertz (1984) set up a quantitative model to explain how a discrete arc is formed by reflected solitary kinetic Alfvén waves.

1.4 Purpose of the project

In contrast with the many theoretical studies of auroral arc formation, there are few published reports which have connected the Alfvén resonances with modulated

auroral luminosity. Higher frequency modulations have been studied by Campbell and Rees (1961), but their frequencies are greater than $10^{-1} Hz$, whereas field line resonances typically have frequencies of 1 - 10 mHz (Samson, 1991a).

In our project, the main purpose is to study the wave behavior of the optical aurora, in order to see variations which might be due to modulation by shear Alfvén waves. We will concentrate on quiet electron auroral arcs in the evening sector before midnight.

Following this research direction, we divide the thesis into five chapters. In Chapter 2 we will discuss how the wave energy can be transferred into the auroral region from the outer magnetosphere. In Chapter 3 we will introduce the data campaign in our project and the experimental methods. The most important observation results will be discussed in Chapter 4. In the last chapter, we evaluate our data by comparing the results with the theoretical model that we have established, and give our final conclusions. Some of the special computational methods and data reduction techniques that we have used in the project are outlined in the appendices.

Chapter Two

THE THEORY OF ULF MHD WAVES IN THE MAGNETOSPHERE

ULF MHD waves in the Earth's magnetosphere are usually called geomagnetic pulsations. These pulsations have frequencies ranging from approximately 1 mHz to greater than 3 Hz and appear as quasisinusoidal oscillations. In this chapter we discuss a theoretical model that explains how compressional MHD waves produced near the low latitude boundary layer of the magnetosphere or the boundary of the plasma sheet are coupled to field line resonance on dipole-like field lines in the inner magnetosphere. We begin our discussion using the set of MHD equations.

2.1 MHD equations in a nonuniform plasma

The MHD equations include mass and momentum conservation, the equation of state, and Maxwell's equations;

$$\frac{\partial \rho}{\partial t} + \nabla \cdot (\rho \mathbf{u}) = 0 \quad (2.1)$$

$$\rho \left(\frac{\partial \mathbf{u}}{\partial t} + (\mathbf{u} \cdot \nabla) \mathbf{u} \right) = -\nabla P + \mathbf{J} \times \mathbf{B} \quad (2.2)$$

$$P \rho^{-\gamma} = \text{constant} \quad (2.3)$$

$$\mathbf{E} + \mathbf{u} \times \mathbf{B} = 0 \quad (2.4)$$

$$\frac{\partial \mathbf{B}}{\partial t} = -\nabla \times \mathbf{E} \quad (2.5)$$

$$\nabla \times \mathbf{B} = \mu_0 \mathbf{J} . \quad (2.6)$$

In these equations, symbols ρ , \mathbf{u} , P , \mathbf{E} , \mathbf{B} and \mathbf{J} respectively represent mass density, fluid velocity, thermal pressure, electric field, magnetic field and current

density. If the unperturbed plasma is in a static equilibrium, the equilibrium components can be written as $\mathbf{u} = 0$, $\mathbf{E} = 0$, $\rho = \rho_0$, $P = P_0$, $\mathbf{J} = \mathbf{J}_0$, $\mathbf{B} = \mathbf{B}_0$.

Linearizing equations (2.1) — (2.6), we get the set of equations for the perturbation field.

$$\frac{\partial \rho_1}{\partial t} + \nabla \cdot (\rho_0 \mathbf{u}_1) = 0 \quad (2.7)$$

$$\rho_0 \frac{\partial \mathbf{u}_1}{\partial t} = -\nabla P_1 + \mathbf{J}_0 \times \mathbf{B}_1 + \mathbf{J}_1 \times \mathbf{B}_0 \quad (2.8)$$

$$\frac{\partial P_1}{\partial t} = -(\mathbf{u}_1 \cdot \nabla) P_0 - \gamma P_0 \nabla \cdot \mathbf{u}_1 \quad (2.9)$$

$$\mathbf{E}_1 + \mathbf{u}_1 \times \mathbf{B}_0 = 0 \quad (2.10)$$

$$\frac{\partial \mathbf{B}_1}{\partial t} = \nabla \times (\mathbf{u}_1 \times \mathbf{B}_0) \quad (2.11)$$

$$\nabla \times \mathbf{B}_1 = \mu_0 \mathbf{J}_1 \quad (2.12)$$

where subscript 1 indicates first order terms. In terms of the displacement vector ξ , $\mathbf{u}_1 = \frac{\partial \xi}{\partial t}$, the equation for ξ is

$$\rho_0 \frac{\partial^2 \xi}{\partial t^2} = -\nabla \tilde{P} + \frac{1}{\mu_0} (\mathbf{B}_1 \cdot \nabla) \mathbf{B}_0 + \frac{1}{\mu_0} (\mathbf{B}_0 \cdot \nabla) \mathbf{B}_1 \quad (2.13)$$

where

$$\tilde{P} = P_1 + \frac{1}{\mu_0} \mathbf{B}_1 \cdot \mathbf{B}_0, \quad (2.14)$$

and

$$\mathbf{E}_1 = \nabla \times (\xi \times \mathbf{B}_0) = (\mathbf{B}_0 \cdot \nabla) \xi - (\nabla \cdot \xi) \mathbf{B}_0 - (\xi \cdot \nabla) \mathbf{B}_0. \quad (2.15)$$

In order to determine the wave equations, we use a cartesian system with variations only in the x direction, *i.e.*

$$B_0 = B_0(x), \quad P_0 = P_0(x), \quad \rho_0 = \rho_0(x), \quad \frac{d}{dx} \left[P_0 + \frac{B_0^2}{2\mu_0} \right] = 0.$$

The zeroth order magnetic field line is in the z direction, but varies in the x direction. Using (2.9), (2.14) and (2.15), we get

$$P_1 = -(\xi \cdot \nabla) P_0 - \rho_0 C_s^2 \nabla \cdot \xi$$

$$\tilde{P} = \rho_0 V_A^2 \frac{\partial \xi_z}{\partial z} - \rho_0 (C_s^2 + V_A^2) \nabla \cdot \xi . \quad (2.16)$$

Here C_s is the sound speed. Substituting (2.15) into (2.13), we get the equation

$$\mu_0 \rho_0 \frac{\partial^2 \xi}{\partial t^2} - (\mathbf{B}_0 \cdot \nabla)^2 \xi = -\mu_0 \nabla \tilde{P} - (\mathbf{B}_0 \cdot \nabla)(\nabla \cdot \xi) \mathbf{B}_0 . \quad (2.17)$$

We can separate equation (2.17) into its three vector components (Roberts, 1984; Kivelson, 1985).

$$\rho_0 \left(\frac{\partial^2 \xi_x}{\partial t^2} - V_A^2 \frac{\partial^2 \xi_x}{\partial z^2} \right) = -\frac{\partial \tilde{P}}{\partial x} \quad (2.18)$$

$$\rho_0 \left(\frac{\partial^2 \xi_y}{\partial t^2} - V_A^2 \frac{\partial^2 \xi_y}{\partial z^2} \right) = -\frac{\partial \tilde{P}}{\partial y} \quad (2.19)$$

$$\frac{\partial^2 \xi_z}{\partial t^2} = C_s^2 \frac{\partial}{\partial z} (\nabla \cdot \xi) . \quad (2.20)$$

If we suppose the displacement vector has the form

$$\xi(\mathbf{r}, t) = \xi(x) e^{i(k_y y + k_z z - \omega t)} ,$$

and define the following characteristic variables,

$$K^2 = k_y^2 + k_z^2$$

$$\omega_s^2 + \omega_f^2 = K^2 (C_s^2 + V_A^2)$$

$$\omega_s^2 \cdot \omega_f^2 = K^2 k_z^2 C_s^2 V_A^2$$

$$C_T^2 = \frac{C_s^2 \cdot V_A^2}{C_s^2 + V_A^2} ,$$

then we find from (2.19) and (2.20) (2.16)

$$\xi_y = \frac{-ik_y (C_s^2 + V_A^2) (\omega^2 - C_T K_z^2)}{(\omega^2 - \omega_s^2) (\omega^2 - \omega_f^2)} \frac{d\xi_x}{dx} \quad (2.21)$$

$$\xi_z = \frac{C_s^2 k_y k_z}{\omega^2 - C_s^2 k_z^2} \xi_y - \frac{ik_z C_s^2}{\omega^2 - C_s^2 k_z^2} \frac{d\xi_x}{dx} \quad (2.22)$$

$$\tilde{P} = \rho_0 V_A^2 ik_z \xi_z - \rho_0 (C_s^2 + V_A^2) [ik_y \xi_y + ik_z \xi_z + \frac{d\xi_x}{dx}] \quad (2.23)$$

Substituting \tilde{P} , ξ_y and ξ_z into (2.18), we finally obtain the differential equation for ξ_x ,

$$\frac{d}{dx} \left[\frac{\rho_0(C_s^2 + V_A^2)(\omega^2 - V_A^2 k_z^2)(\omega^2 - C_T^2 k_z^2)}{(\omega^2 - \omega_s^2)(\omega^2 - \omega_f^2)} \frac{d\xi_x}{dx} \right] + \rho_0(\omega^2 - V_A^2 k_z^2)\xi_x = 0 . \quad (2.24)$$

If the plasma is uniform, the equation gives two simple dispersion relations.

The first is

$$\omega^2 - k_z^2 V_A^2 = 0 .$$

This is a shear Alfvén wave propagating along the field line. The second dispersion relation is

$$(\omega^2 - \omega_s^2)(\omega^2 - \omega_f^2) = 0 ,$$

$$\omega^4 - \omega^2(V_A^2 + C_s^2)K^2 + C_s^2 V_A^2 K^4 \cos^2 \theta = 0 .$$

Here $k_z^2 = K^2 \cos^2 \theta$, and θ is the angle between the magnetic field and the wave vector. We finally get the phase velocity of the waves.

$$\frac{\omega_{\pm}^2}{K^2} = \frac{1}{2}(C_s^2 + V_A^2) \left[1 \pm \sqrt{1 - \frac{4C_s^2 V_A^2 \cos^2 \theta}{(C_s^2 + V_A^2)^2}} \right]$$

$$\omega_{\pm}^2 = K^2 V_{p\pm}^2 .$$

When $\cos \theta \ll 1$ or $C_s \ll V_A$ or $V_A \ll C_s$,

$$V_f^2 = V_{p+}^2 \approx C_s^2 + V_A^2 ,$$

and

$$V_s^2 = V_{p-}^2 \approx \frac{C_s^2 V_A^2}{C_s^2 + V_A^2} \cos^2 \theta .$$

These velocities are usually associated with fast and slow waves, and satisfy the following inequality

$$V_s < V_A < V_f .$$

In a nonuniform plasma, the differential equation (2.24) has two turning points and two resonances. The resonances, occurring where $\omega^2 = k_z^2 V_A^2$, $k_z^2 C_T^2$,

are singularities of the differential equation. There are no regular solutions at these points. The compressional wave energy will be absorbed at these points. ω_s and ω_f in the equation (2.24) are turning points, or cut-off points (Roberts, 1984). At such points, the behavior of the waves changes from an oscillating form to an evanescent form.

2.2 MHD waves in the magnetosphere

2.2.1 Southwood-Chen-Hasegawa theoretical model

In a cold nonuniform plasma ($\beta = \frac{\mu_0 P}{B^2} \ll m_e/m_i$), the thermal pressure is negligible and there are no propagating magnetosonic waves in the plasma. Then equation (2.24) has the form (Chen and Hasegawa, 1974a; 1974b),

$$\frac{d}{dx} \left[\frac{\varepsilon B_0^2}{k_y^2 B_0^2 - \varepsilon} \frac{d\xi_x}{dx} \right] - \varepsilon \xi_x = 0 \quad (2.25)$$

where $\varepsilon(x) = \mu_0 \rho_0 (\omega^2 - k_z^2 V_A^2)$. In the large k_y approximation, we may simplify equation (2.25) near x_0 , the resonant position, to give

$$\frac{d^2 \xi_x}{dx^2} + \frac{1}{\varepsilon} \frac{d\varepsilon}{dx} \frac{d\xi_x}{dx} - k_y^2 \xi_x = 0 \quad (2.26)$$

This equation has only one resonance ($\varepsilon(x_0) \approx 0$) and no turning point. If $k_y = 0$, then equation (2.25) becomes

$$\frac{d^2 \xi_x}{dx^2} + \left(\frac{\omega^2}{V_A^2} - k_z^2 \right) \xi_x = 0 \quad (2.27)$$

Equation (2.27) has only a linear turning point at $\omega^2 = V_A^2 k_z^2$. In this case, it implies a total reflection of an incident wave at the turning point (Stix, 1962).

If k_y is a finite number, we expand $\varepsilon(x)$ near the resonant point x_0 , giving,

$$\varepsilon(x) = \varepsilon_r(x_0) + (x - x_0) \frac{d\varepsilon_r}{dx} + i\varepsilon_i(x_0) \quad .$$

Here $\varepsilon_r, \varepsilon_i$ are respectively the real and imaginary part of $\varepsilon(x)$. We further define a damping factor of the wave

$$\gamma' = \frac{\varepsilon_i}{\frac{\partial \varepsilon_r}{\partial x}} \quad (\varepsilon_i \ll \varepsilon_r).$$

Then, near the resonance, equation (2.25) becomes

$$\frac{d^2 \xi_x}{dx^2} + \frac{1}{(x - x_0) + i\gamma'} \frac{d\xi_x}{dx} - k_y^2 \xi_x = 0. \quad (2.28)$$

The approximate solution is

$$\xi_x = c \exp[ik_y(x - x_0 + i\gamma')]. \quad (2.29)$$

Equations (2.27) and (2.28) are used to describe two limiting cases, $k_y \rightarrow 0$ and k_y is a large number. In the latter situation, Chen and Hasegawa (1974a, 1974b) set up two theoretical models, one assuming the steady state excitation of field line resonances due to the energy from Kelvin-Helmholtz instabilities on the magnetopause, the another assuming the impulse excitation of surface eigenmodes at a plasma discontinuity (for example, the plasmopause).

2.2.2 Global models

Kivelson and Southwood (1985) first provided a global model to explain the wave mode coupling process in the MHD scenario. They used the first order disturbed magnetic field (B_{1z}) in the zero magnetic field direction in their differential equation (Kivelson and Southwood, 1985; 1986). In their study they found that the MHD equation was similar to that for an EM wave propagating in the ionosphere (Budden, 1961). Considering, again, a cold plasma condition, and letting $B_0 = \text{constant}$, from equations (2.16), (2.18), (2.19) and (2.20), we have

$$(k_z^2 - \frac{\mu_0 \rho_0}{B_0^2} \omega^2) \xi_x = -\frac{1}{B_0} \frac{\partial B_{1z}}{\partial x} \quad (2.30)$$

$$(k_z^2 - \frac{\mu_0 \rho_0}{B_0^2} \omega^2) \xi_y = -i k_y \frac{B_{1z}}{B_0} \quad (2.31)$$

$$B_{1z} = -i k_y B_0 \xi_y - B_0 \frac{\partial \xi_x}{\partial x} . \quad (2.32)$$

Substituting ξ_y in (2.32) into (2.30), (2.31) gives

$$(k_z^2 + k_y^2 - \frac{\mu_0 \rho_0}{B_0^2} \omega^2) B_{1z} + (k_z^2 - \frac{\mu_0 \rho_0}{B_0^2} \omega^2) B_0 \frac{\partial \xi_x}{\partial x} = 0 . \quad (2.33)$$

Equation (2.33) includes a wave coupling process, giving a coupling relation between the compressible component B_{1z} and the displacement of the magnetic field line, ξ_x . Differentiating (2.30) with respect to x , gives

$$(k_z^2 - \frac{\mu_0 \rho_0}{B_0^2} \omega^2) \frac{\partial \xi_x}{\partial x} + [\frac{\partial}{\partial x} (k_z^2 - \frac{\mu_0 \rho_0}{B_0^2} \omega^2)] \xi_x = -\frac{1}{B_0} \frac{\partial^2 B_{1z}}{\partial x^2} . \quad (2.34)$$

Using (2.30) and (2.33) and substituting into (2.34) to eliminate ξ_x and $\frac{\partial \xi_x}{\partial x}$, we finally obtain the equation

$$\frac{d^2 B_{1z}}{dx^2} - \frac{1}{k_z^2 - \frac{\omega^2}{V_A^2}} \left[\frac{d}{dx} (k_z^2 - \frac{\omega^2}{V_A^2}) \right] \frac{dB_{1z}}{dx} - [k_y^2 + (k_z^2 - \frac{\omega^2}{V_A^2})] B_{1z} = 0. \quad (2.35)$$

In this model, Kivelson and Southwood (1986) pointed out that the global compressional eigenmodes are quantized by the radial structure of the magnetosphere. They used this model and a given k_y which depends on the azimuthal size of the cavity to produce monochromatic frequencies. They also pointed out that the wave mode is changed at the resonant point, coupling to the shear Alfvén mode, in the region where the compressional mode decays exponentially (the non-propagating side of the turning point). The coupling coefficient depends on the gradient of plasma distribution and azimuthal wave number k_y .

2.3 WKB solutions in nonuniform plasma

In order to analyze WKB solutions, we first assume a linear plasma profile in the unbounded plasma that has $\frac{\omega^2}{V_A^2} = \alpha^2 x$, $k_z^2 = \alpha^2 x_0$, $k_y^2 = \alpha^2 x_\lambda$, (Kivelson and Southwood, 1986).

Here α^2 is a positive constant that determines the gradient of the plasma distribution. x_0 and x_λ are respectively the resonant point and turning point. Equation (2.35) becomes

$$\frac{d^2 B_{1z}}{dx^2} - \frac{1}{x - x_0} \frac{dB_{1z}}{dx} + \alpha^2(x - x_0 - x_\lambda)B_{1z} = 0. \quad (2.36)$$

We can further simplify the equation by using the variables (Budden, 1961; Denisov, 1957). $(x - x_0)\alpha^{\frac{2}{3}} = -\zeta$, $q = x_\lambda\alpha^{\frac{2}{3}} = k_y^2\alpha^{-\frac{4}{3}}$. Then equation (2.36) becomes

$$\frac{d^2 B_{1z}}{d\zeta^2} - \frac{1}{\zeta} \frac{dB_{1z}}{d\zeta} - (\zeta + q)B_{1z} = 0. \quad (2.37)$$

Let $B_{1z} = G\zeta^{\frac{1}{2}}$, then

$$\frac{d^2 G}{d\zeta^2} - (\zeta + q + \frac{3}{4\zeta^2})G = 0. \quad (2.38)$$

Finally let

$$P^2 = (\zeta + q + \frac{3}{4\zeta^2}) \quad (2.39)$$

and equation (2.38) is simplified to

$$\frac{d^2 G}{d\zeta^2} = P^2 G. \quad (2.40)$$

We now find its WKB solution. Let

$$G = Ae^{i\phi(\zeta)} \quad (2.41)$$

giving

$$\frac{d^2 G}{d\zeta^2} = G\{i\frac{d^2\phi}{d\zeta^2} - (\frac{d\phi}{d\zeta})^2\}. \quad (2.42)$$

Substituting (2.41) into (2.40) gives

$$(\frac{d\phi}{d\zeta})^2 = -P^2 + i\frac{d^2\phi}{d\zeta^2}. \quad (2.43)$$

Using the condition

$$\frac{d^2\phi}{d\zeta^2} \ll (\frac{d\phi}{d\zeta})^2 \quad (2.44)$$

so that

$$\frac{d\phi}{d\zeta} \approx \pm iP$$

gives

$$\frac{d^2\phi}{d\zeta^2} = \pm i \frac{dP}{d\zeta} .$$

Substituting the above equation into (2.43) gives

$$\left(\frac{d\phi}{d\zeta}\right)^2 = -P^2 \mp \frac{dP}{d\zeta} , \quad (2.45)$$

and

$$\phi = \pm \int^{\zeta} iP d\zeta + i \ln(P^{\frac{1}{2}}) . \quad (2.46)$$

We finally get

$$G = AP^{\frac{1}{2}} \exp\{\mp \int^{\zeta} P d\zeta\}$$

and

$$B_{1z} = A\zeta^{\frac{1}{2}} \left(\zeta + q + \frac{3}{4\zeta^2}\right)^{-\frac{1}{4}} \exp\{\mp \int^{\zeta} \left(\zeta + q + \frac{3}{4\zeta^2}\right)^{\frac{1}{2}} d\zeta\} . \quad (2.47)$$

The expression is an asymptotic solution that is only suitable for regions far from the turning point and resonance. Equation (2.37) has a singular point at $\zeta = 0$, corresponding to the resonance. At this point the WKB solution is invalid (Budden, 1961).

The second singular point of the WKB solution occurs where $P = 0$. It corresponds to a turning point. When P is equal to zero, the solution of B_{z1} is also infinite. Here we would like to point out that the singularity is purely a result of the WKB method itself. In the original equation (2.38) $P = 0$ is a linear regular point.

2.4 Numerical solutions for the coupled model with tunnelling

In this section, we outline our coupled model with tunnelling. The model is different from Southwood-Chen-Hasegawa model, the global cavity, and box models. We use a travelling wave model suitable for the magnetospheric flank region. In the x direction, we make an assumption that there is a compressional wave produced at the low latitude boundary layer propagating toward Earth. We select a natural boundary, where all of the components are continuous. We use the WKB method to address asymptotic solutions matching suitable boundary conditions. In the y direction, we assume a y dependence of the form $e^{ik_y y}$. The value of k_y has a strong influence on the amount of coupling between the compressional and shear Alfvén waves. It is also an important parameter to determine the resonant width of the Alfvén wave. In this model, we use a numerical method to determine the value of k_y that corresponds to the maximum coupling coefficient of the system; then we give the general solution for the system. The schematic representation of the tunnel coupling model is plotted in Figure 2.1.

2.4.1 The complex solution of the differential equation

In order to obtain a numerical solution, we shall expand equation (2.36) into a set of first order ordinary differential equations (Budden, 1961). From equation (2.30) we obtain

$$\frac{dB_{1z}}{dx} = B_0 \alpha^2 (x - x_0) \xi_x, \quad (2.48)$$

and (2.36) becomes

$$\frac{d\xi_x}{dx} = -\frac{1}{B_0} \frac{x - x_0 - x_\lambda}{x - x_0} B_{1z}. \quad (2.49)$$

Finally the above two equations can be changed to

$$\frac{dB_{1z}}{d\zeta} = B_0 \alpha^{\frac{2}{3}} \zeta \xi_x \quad (2.50)$$

$$\frac{d\xi_r}{d\zeta} = \frac{\alpha^{-\frac{2}{3}}}{B_0} \left(\frac{\zeta + q}{\zeta} \right) B_{1z}, \quad (2.51)$$

Normalizing, $Y_1 = B_{1z}$, $Y_2 = B_0 \alpha^{\frac{2}{3}} \xi_r$, $Y_3 = B_0 \alpha^{\frac{2}{3}} \xi_y$, gives

$$\frac{dY_1}{d\zeta} = \zeta Y_2, \quad (2.52)$$

$$\frac{dY_2}{d\zeta} = \frac{\zeta + q}{\zeta} Y_1, \quad (2.53)$$

and from (2.31),

$$Y_3 = -i \frac{q^{\frac{1}{2}}}{\zeta} Y_1. \quad (2.54)$$

This is a set of first order complex ordinary differential equations. We have to solve the equation on the complex ζ plane. We already know that Y_1 has a WKB solution of the form

$$Y_1 = k \zeta^{\frac{1}{2}} (\zeta + q)^{-\frac{1}{4}} \exp \left\{ \pm \frac{2}{3} \left(\zeta + q + \frac{3}{4\zeta^2} \right)^{\frac{3}{2}} \right\}. \quad (2.55)$$

This is an asymptotic solution which is valid far from the resonance and turning point. Depending on our choice of variables, we can figure out a physics picture for the problem. On the complex ζ plane, the compressional wave propagates toward the high Alfvén velocity region on the real axis of $\arg \zeta = \pi$ from left to right (see Figure A.1 in the appendix). It first meets the turning point at $\zeta = -q$, and part of the wave energy should be reflected. Next, the part of the wave passing through the reflection point, $\zeta = -q$, will continue to propagate to the resonant point, $\zeta = 0$, where its energy is coupled to shear Alfvén waves. After the point $\zeta = 0$, toward the $\arg \zeta = 0$ direction, there is a dissipative region. None of wave energy can leak out of the region.

Based on the physical picture above, we can constitute two asymptotic solution on both sides of the $\zeta = 0$ region. These are given by a connection formula (Budden, 1961; Piliya, 1965; Hirsch, 1966; Speziale, 1976; Ott, 1978),

$$k \zeta^{\frac{1}{2}} (\zeta + q)^{-\frac{1}{4}} \left\{ e^{[-\frac{2}{3}(\zeta+q)^{\frac{3}{2}}]} + \Re e^{[\frac{2}{3}(\zeta+q)^{\frac{3}{2}}]} \right\} \iff k \zeta^{\frac{1}{2}} (\zeta + q)^{-\frac{1}{4}} e^{[-\frac{2}{3}(\zeta+q)^{\frac{3}{2}}]}, \quad (2.56)$$

Here \mathfrak{R} is called the Stokes constant. The first term of the solution on the left side indicates an incident wave, and the second term a reflected wave. If $q = 0$, the Stokes constant, $\mathfrak{R} = i$. Therefore, we can say that the asymptotic behavior of our problem is exactly similar with the Stokes equation (Budden, 1961), but the Stokes constant will be a complex number with its absolute value being equal to or less than 1, depending on the magnitude of parameter q .

We can follow the method of Budden (1961) to determine a reflection coefficient R , the ratio of the amplitude of the wave reflected from the turning point to the incident wave. Based on the WKB solutions, the phase integral formula of R can be written as

$$R = \mathfrak{R} \exp\left\{-2 \int^{\zeta} \left(\zeta + q + \frac{3}{4\zeta^2}\right)^{\frac{1}{2}} d\zeta\right\}. \quad (2.57)$$

On the complex ζ plane, if a wave is moving along the $\arg \zeta = \pi$ axis toward the reflection point $-q$, the exponential part of R will be a pure imaginary number. Therefore, $|R| = |\mathfrak{R}|$, and if we can determine the Stokes constant, we can determine the reflection coefficient and the absorption of the wave.

On the other hand, the existence of an imaginary part in \mathfrak{R} has a special meaning in the region to the left of the reflection point $\zeta = -q$. In this region the asymptotic solution (2.56) shows that the exponential parts of the two terms on the left hand side of the equation are purely imaginary if $\arg \zeta = \pi$. If the Stokes constant has an imaginary part, it means the reflected wave includes a wave component that has a 90° phase shift. Under this scenario, the reflected wave will form a wave field similar to a standing wave.

In order to link the asymptotic solutions, we follow Budden's method. First we separate the ζ complex plane into several different regions. There is a Stokes line at $\arg \zeta = 0$, $\arg \zeta = \frac{2\pi}{3}$, and an anti Stokes line at $\arg \zeta = \frac{\pi}{3}$ and $\arg \zeta = \pi$ in Figure A.1.

The asymptotic solution on the right side of the formula (2.56) is appropriate in the region $0 \leq \arg \zeta \leq \frac{\pi}{3}$. It is called the dominant term in the Stokes solution. When the solution crosses the anti Stokes line at $\arg \zeta = \frac{\pi}{3}$, it becomes the subdominant term with $\arg \zeta$ increasing. From $\arg \zeta = \frac{\pi}{3}$ to $\arg \zeta = \pi$, the solution will cross the Stokes line $\arg \zeta = \frac{2\pi}{3}$. On the line, the solution has its maximum value, and the Stokes phenomenon occurs. The solution on the far left side of the region should have two terms in which the subdominant terms will multiply the Stokes constant.

In this project, in order to determine \Re , which depends on q , we use a numerical method. We have selected the integration length $r = \sqrt{3}d$, and $d = 12$, and used a fourth order Runge-Kutta integrator to advance the solution of the equation until $\arg \zeta = \pi$. Our numerical result is very similar to the solution of Budden (1961). The reflection coefficient R has a minimum value at the coupling parameter $q = 0.537$. Since the absorption coefficient $A = 1 - R^2$, it also gives maximum absorption. The absorption coefficient is plotted in Figure 2.2. Figures 2.3 to 2.6 are numerical solutions of the ODE that are obtained by integrating on the real axis. The discontinuity at $\zeta = 0$ corresponds to the position of the resonance. The turning point is located at $\zeta = -0.537$, corresponding to coefficient $q = 0.537$.

2.4.2 Resonant absorption and energy absorption rate

From our one dimensional model, the energy absorption rate $\frac{dW}{dt}$ in the x direction can be calculated from (Chen and Hasegawa, 1974)

$$\frac{dW}{dt} = \frac{1}{2} L_y L_z \langle \mathbf{P} \rangle \cdot \mathbf{e}_x .$$

Here L_y and L_z are the size of plasma in the y and z directions, and \mathbf{e}_x is the unit vector in the x direction. If we consider the energy absorption on a unit area that

is perpendicular to the x direction,

$$\frac{dW}{dt} = \frac{1}{2} \text{Re}[\mathbf{P}_{x_1} - \mathbf{P}_{x_2}], \quad (2.58)$$

where \mathbf{P} is the Poynting vector

$$\mathbf{P} = \frac{1}{\mu_0} \mathbf{E}^* \times \mathbf{B}_{1z},$$

and

$$\mathbf{E} = -\mathbf{u}_1 \times \mathbf{B}_0 = i\omega B_0 \xi \times \mathbf{e}_z.$$

\mathbf{E} is perpendicular to background magnetic field $B_0 \mathbf{e}_z$. Only b_z and E_y contribute to the Poynting vector. Substituting $E_y = i\omega \xi_x B_0$ into (2.58) gives

$$\begin{aligned} \frac{dW}{dt} &= -\frac{1}{2} \frac{\omega}{\mu_0} \text{Re} \left\{ i[B_0 B_{1z} \xi_x^*]_{x_1} - i[B_0 B_{1z} \xi_x^*]_{x_2} \right\} \\ &= \frac{1}{2} \frac{\omega}{\mu_0} \text{Im} \{ B_0 B_{1z} \xi_x^* \}_{x_1}^2. \end{aligned} \quad (2.59)$$

From our numerical solution,

$$\frac{dW}{dt} = \frac{\alpha^{-\frac{2}{3}} \omega}{2 \mu_0} \text{Im} [Y_1 Y_2^*]_{\zeta_1}^2. \quad (2.60)$$

Expression (2.60) shows that the energy absorption in the resonance region is determined only by the solution of Y_1 and Y_2 , on both sides of the resonance position. Furthermore, the asymptotic solution of (2.56) on the right side of the resonant point shows an exponential decrease. Therefore, the total energy passing the turning point will be deposited in the resonance.

2.5 Kinetic Alfvén waves and auroral electrons

There are numerous theoretical studies concerning the effects of small scale sizes on the resonance and the need to treat the shear Alfvén waves in the more accurate kinetic Alfvén wave approximation. These kinetic Alfvén waves might be associated with auroral particle precipitation (Hasegawa, 1976, 1990; Goertz, 1979,

1984). The kinetic effects become important when the width of the resonance region becomes comparable to the ion gyroradius ($\beta > m_e/m_i$) or the electron inertial length ($\beta < m_e/m_i$). The kinetic effects lead to the kinetic Alfvén wave which has a finite parallel electric field that can accelerate electrons along magnetic field lines. In a collisionless plasma like that in the magnetosphere, wave particle interaction leads to Landau damping of the kinetic Alfvén waves.

Hasegawa (1976) and Goertz (1984) studied kinetic effects in the mode conversion of compressional Alfvén waves to kinetic Alfvén wave. They give the equation of the radial electric field E_r ,

$$D_{\pm}^2 \frac{d^2 E_r}{dx^2} \pm Kx E_r = E_0 \quad (2.61)$$

where the x-component is perpendicular to the magnetic field in the radial direction and they assumed a linear density profile, giving the Alfvén velocity $V_A^2(x) = V_{A0}^2/(1 + Kx)$. In equation (2.61)

$$D_+^2 = \left(\frac{3}{4} + \frac{T_e}{T_i}\right)r_{gi}^2 \quad 1 > \beta > m_e/m_i \quad (2.62)$$

and

$$D_-^2 = c^2/\omega_{pe}^2 \quad \beta < m_e/m_i \quad (2.63)$$

where r_{gi} is the ion gyroradius. The kinetic Alfvén wave propagates into the denser medium of the plasma if the plasma is "warm" $\beta > m_e/m_i$ or into the more tenuous plasma if the plasma is cold $\beta < m_e/m_i$. Away from the position of the resonance, the kinetic Alfvén wave has a perpendicular wavelength $\lambda_{\perp} \approx (3\pi)^{\frac{2}{3}}(D^2/K)^{\frac{1}{3}} \approx (2\pi/k_x)$. In a warm plasma these wavelength are comparable to the ion gyroradius and would likely be only 10's of km when mapped to the auroral region in the ionosphere.

Goertz (1981) separates the Alfvén waves, depending on their perpendicular wavelength, into two categories. The small perpendicular wavelength that is

less than plasma skin depth c/ω_{pe} has short time scale and may cause detached break-up arcs. He has also shown that multiple reflections of the Alfvén waves can lead to electric field configurations similar to those causing inverted V electron precipitation. In chapter 5 of the thesis, we will discuss this possibility on the basis of our data analysis.

Tunnel Coupling Model in Flank Region of the Magnetosphere

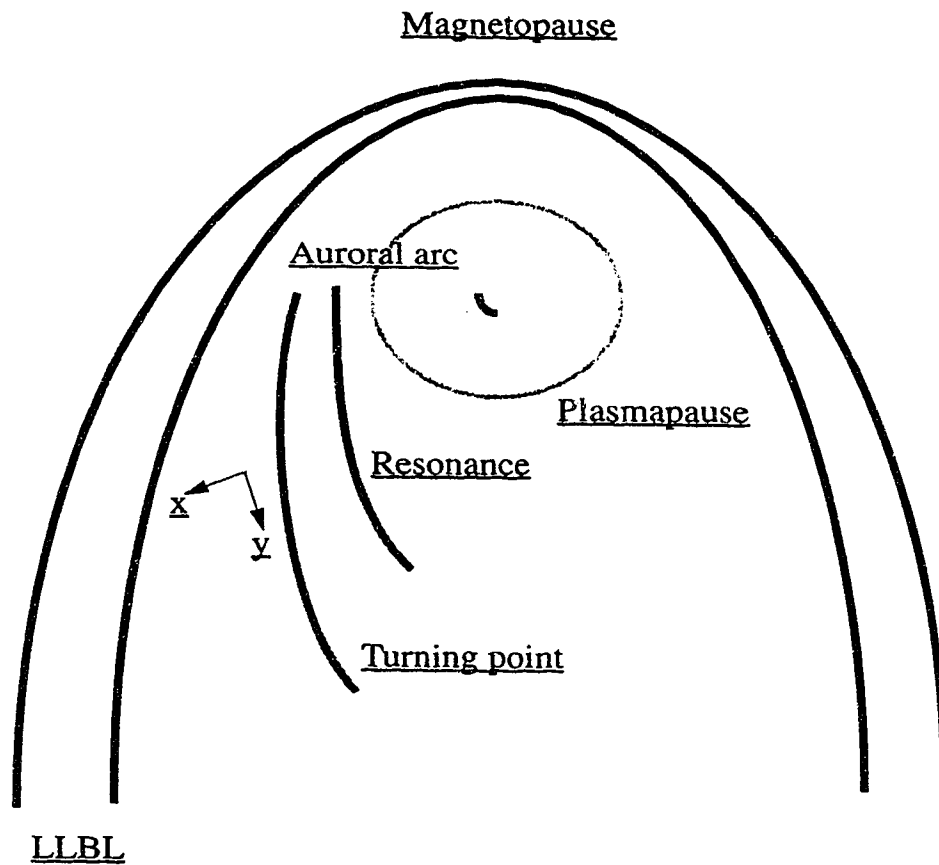


Figure 2.1: Schematic representation for tunnel coupling model in the flank region of the magnetosphere.

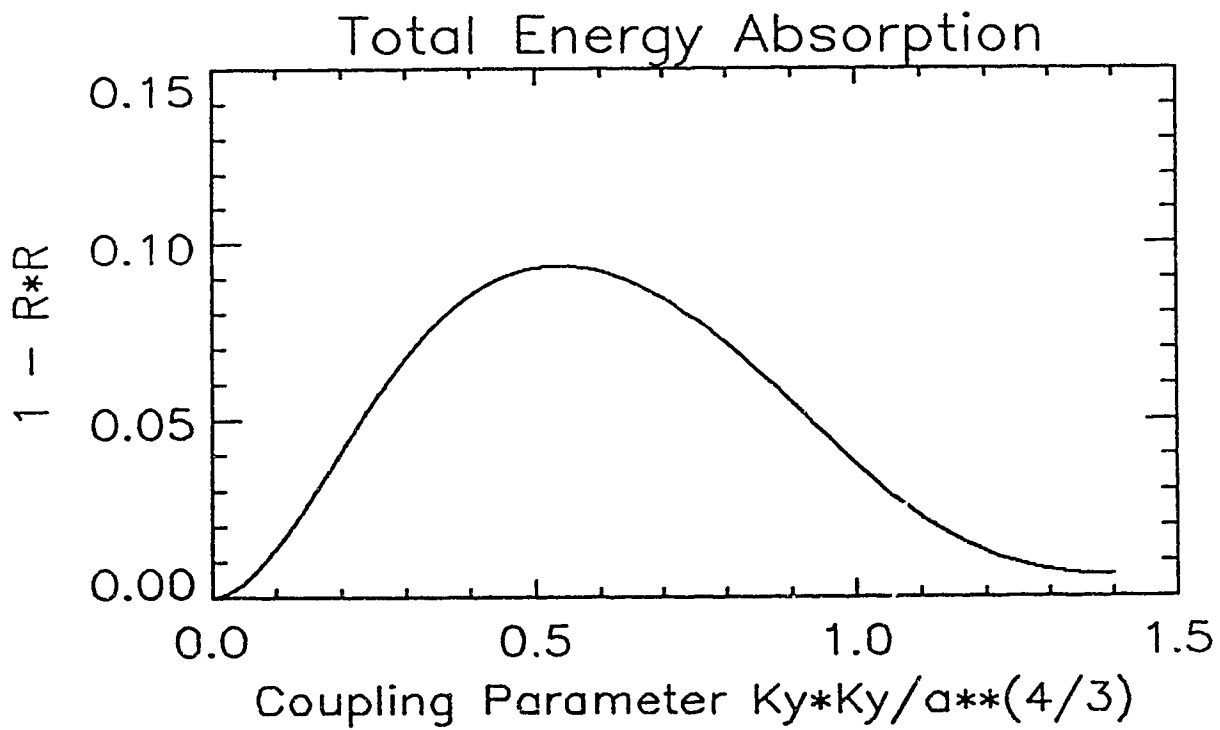


Figure 2.2: The energy absorption coefficient in the resonant Alfvén wave region plotted against the coupling parameter q . The maximum occurs at $q = 0.537$.

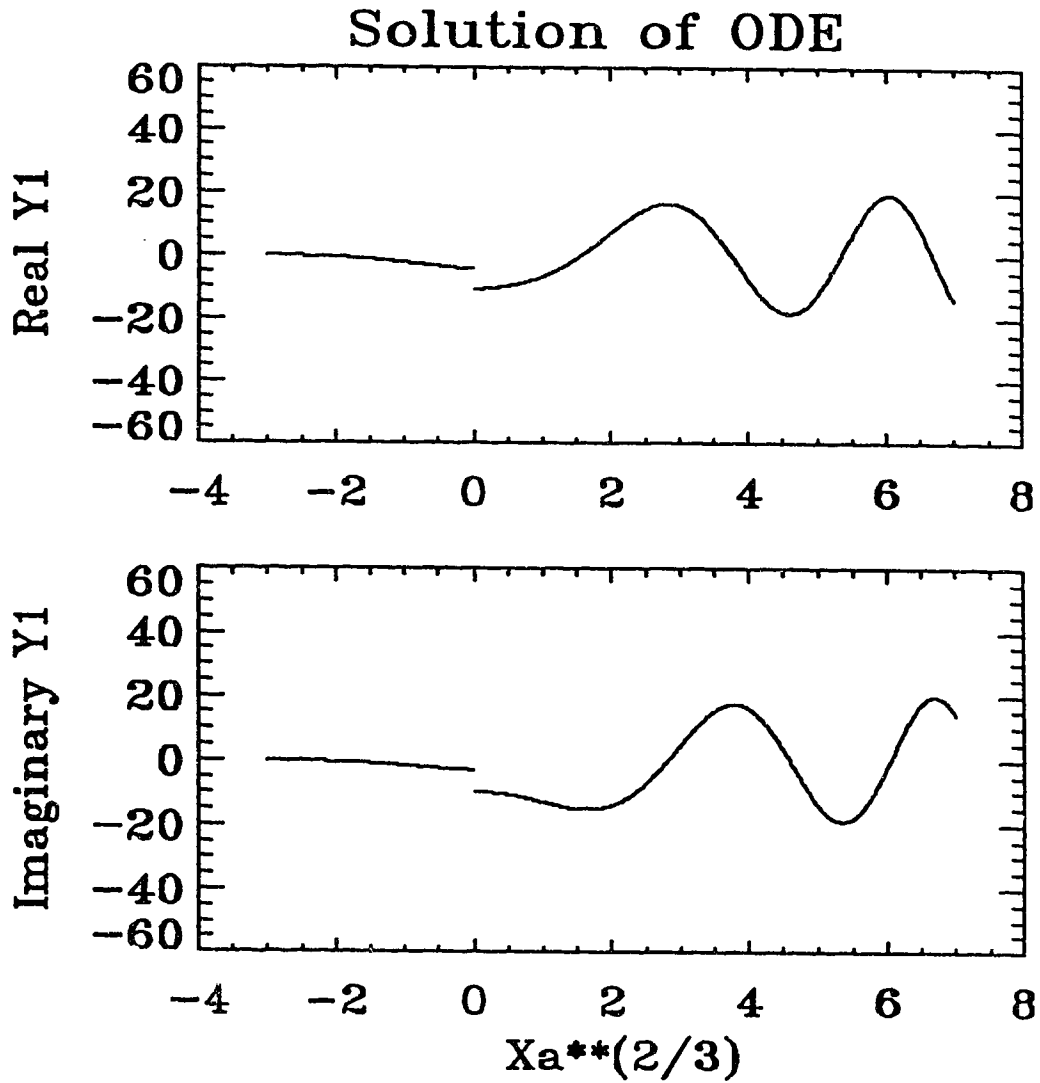


Figure 2.3: Numerical solutions for Y_1 , where Y_1 is the normalized disturbed magnetic field B_{1z} . The incident wave propagates from right to left. The solution is obtained with the coupling coefficient $q = 0.537$, corresponding to the largest absorption. Resonant absorption occurs at the origin, and the compressional component Y_1 gives a discontinuity where the energy transfers into the resonant field line oscillation.

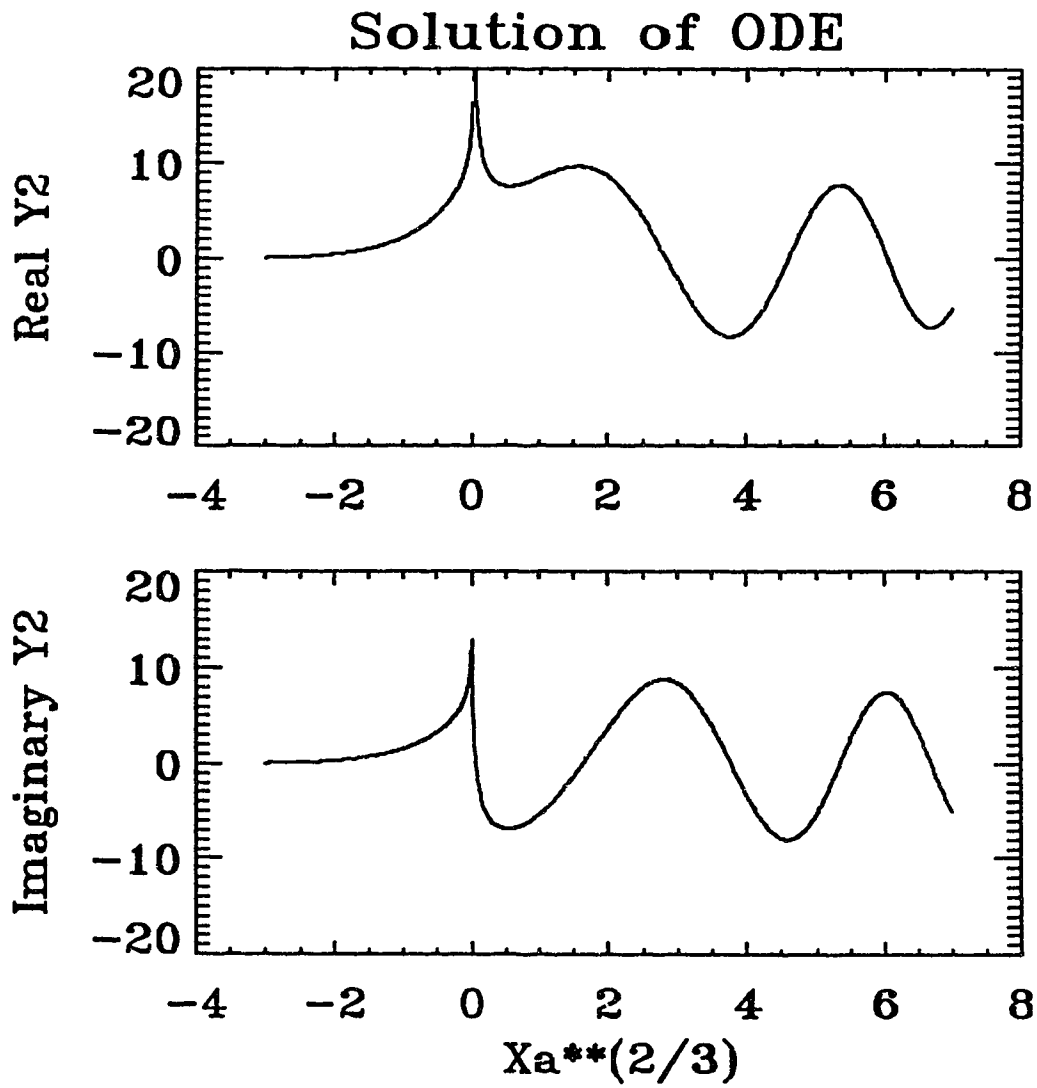


Figure 2.4: Numerical solutions for Y_2 , where Y_2 is the normalized field line displacement ξ_x . The solution is obtained with the coupling coefficient $q = 0.537$ corresponding to the largest absorption. The large spike at origin marks the position of resonant absorption.

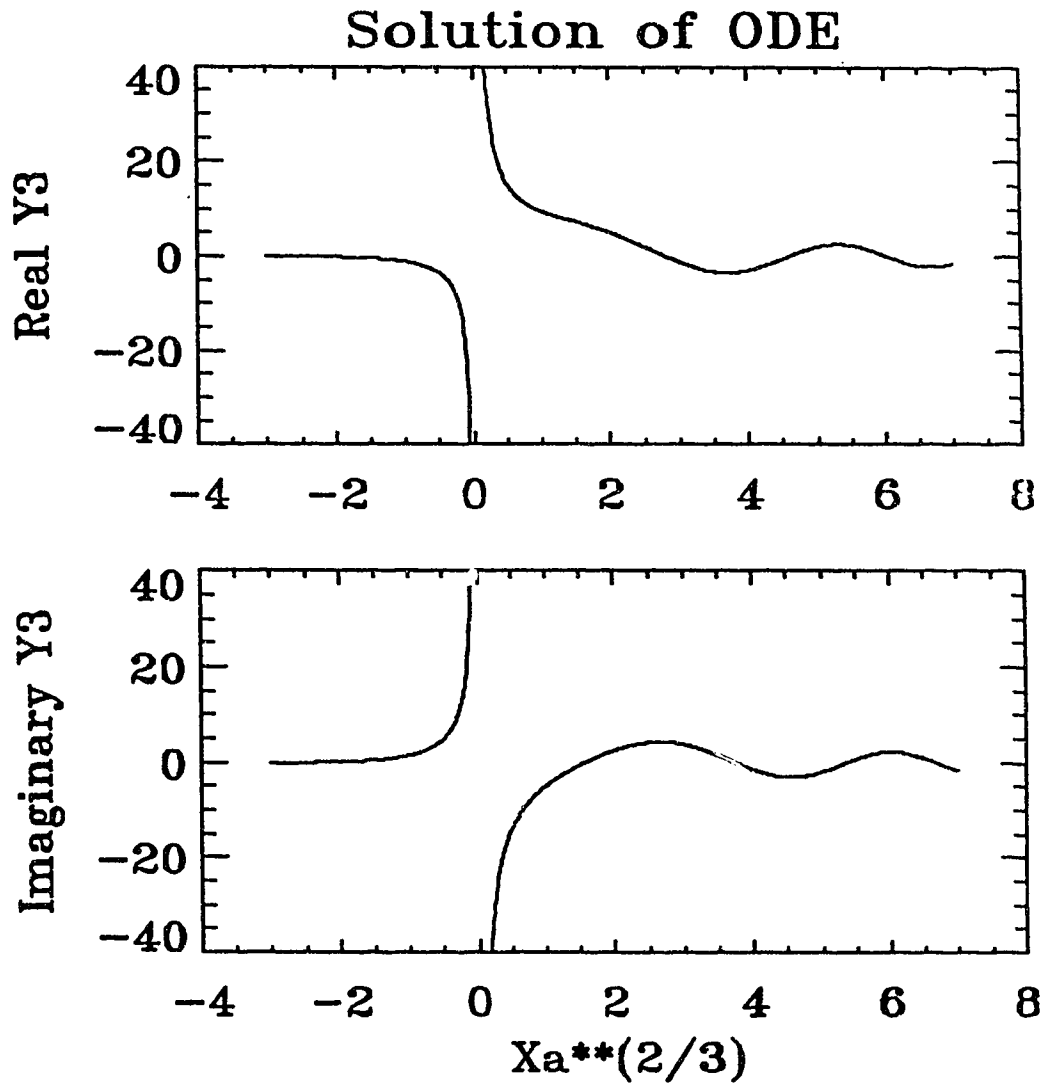


Figure 2.5: Numerical solutions for Y_3 , where Y_3 is the normalized field line displacement ξ_y . The solution is obtained with the coupling coefficient $q = 0.537$ corresponding to the largest absorption.

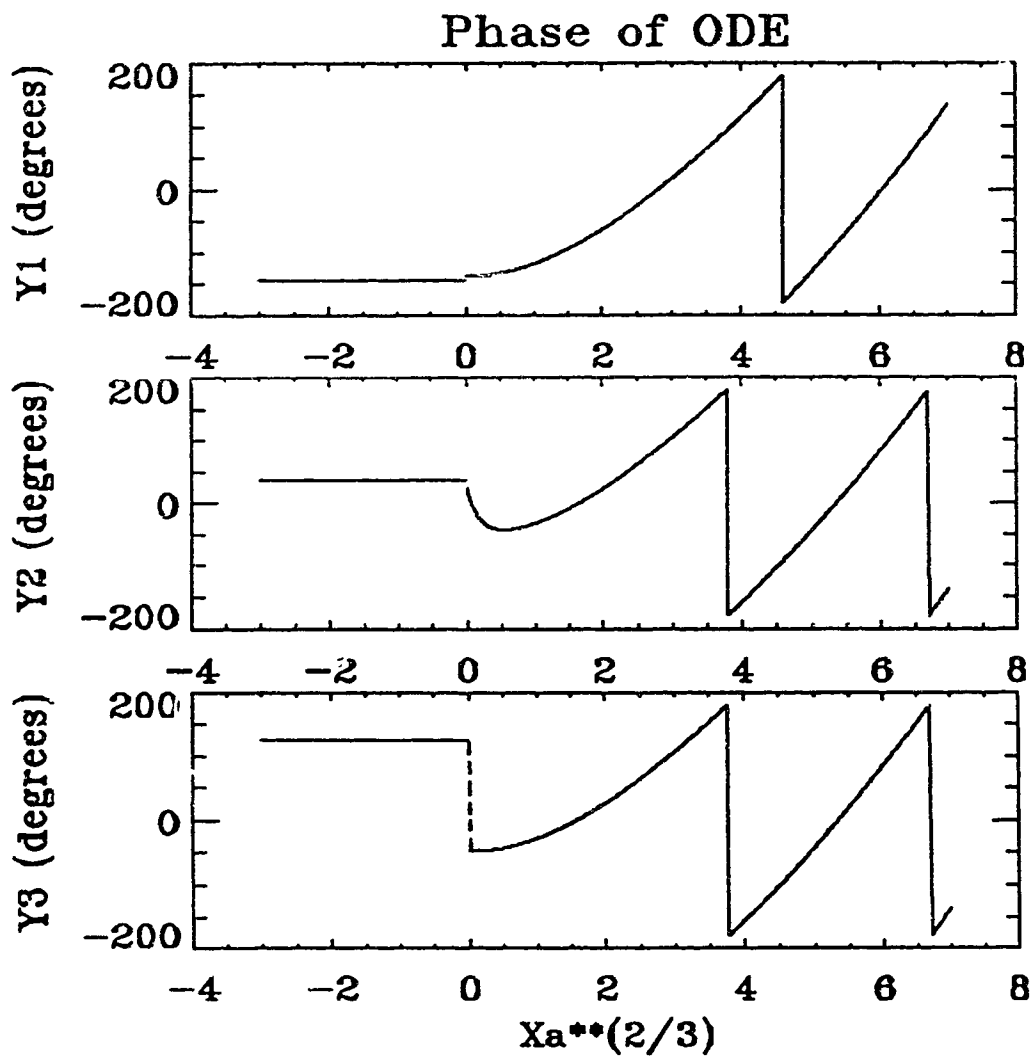


Figure 2.6: Phases of normalized Y_1 , Y_2 and Y_3 . Y_2 and Y_3 have an inverted phase change at the turning point.

Chapter Three

INSTRUMENTATION AND METHODS

3.1 CANOPUS — the data campaign in our project

In this project we use the data obtained by the CANOPUS array of ground based instruments (Vallance Jones, 1982). The name of the array was originally an acronym based on the Canadian Auroral Network for the Open Unified Study. It was a component of the NASA OPEN program. The CANOPUS system provides the key data base to describe the processes involving the coupling of the magnetosphere and ionosphere through electric fields and currents. The network includes riometers, magnetometers, meridian scanning photometers, a bistatic auroral radar, and an all sky imager. In our project, we use the magnetometer and meridian scanning photometer data to study auroral arcs and the magnetic fields associated with ULF plasma waves in the ionosphere and magnetosphere.

3.1.1 Meridian Photometer Array (MPA)

The CANOPUS array of photometers measure meridian profiles of the 5577 Å, 6300 Å, 4709 Å, and 4861 Å H_j emissions. In the CANOPUS system there are eastern and western meridian scanning photometer lines, located respectively on the geographic coordinate 92°42'(W) meridian and 111°58'(W) meridian. In our analysis, we only use data from the eastern line of photometers. The eastern line consists of three photometers, Rankin Inlet (73.54° Invariant latitude), Gillam (67.18° Invariant latitude) and Pinawa (60.95° Invariant latitude). The three instruments permit complete overlapping coverage over a large range of latitudes, from approximately 55° to 76° Invariant Latitudes. This covers the range of

latitudes where Alfvén wave field line oscillation associated with auroral particle precipitation occurs (Lam and Rostoker, 1978; Olson and Rostoker, 1980, Samson, 1991a; 1991b).

The photometer array consists of meridian scanning, eight-channel filter-wheel photometers. Five of the eight channels measure auroral emissions in 4709 Å, 4861 Å (twice), 5577 Å, and 6300 Å. Another three channels measure background emissions in 4800 Å, 4935 Å, and 6250 Å. Each instrument scans the meridian at two revolutions per minute with a sampling rate of 510 samples per scan per channel. The data from each scan are averaged into 17 latitudinal bins for each line. Due to the fact that different auroral emission lines occur at different heights, we have to choose an average emission height for each line. In the CANOPUS system, the average height of emissions of the 5577 Å, 4861 Å and 4709 Å lines are selected to be at 110 km above the Earth's surface, and the average height of the 6300 Å line is selected to be at 230 km. Table 3.1 gives the relation between bin numbers and latitudes for the photometer.

3.1.2 Magnetometer and Riometer Array (MARIA)

MARIA consists of an array of 12 magnetometers and 12 riometers. Figure 3.1 shows the positions of the 7 stations used in our study. The closely spaced north-south magnetometer line near Hudson Bay permits identification of the poleward and equatorward boundaries of the auroral electrojets in the ionosphere. The magnetometers record 3 components (X, Y, Z) where X is geographic north, Y is geographic east, and Z is positive downward. The X-direction is within 3° of the geomagnetic north direction for our observation stations. The locations of the magnetometer stations we have used in the project are listed in Table 3.2.

The riometers are used to monitor extremely high energetic particle precipitation, usually 10 - 100 keV electrons (Berkey, 1974). In our project, we are

concerned with lower energy electrons, typically several keV or less and consequently the riometers are not useful for this study.

3.2 Objectives and method

3.2.1 Parameters observed in the project

In the first chapter of this thesis, we indicated that the essence of the project is to study the relation between resonant Alfvén waves and auroral arcs. Both phenomena have similar features including narrow latitudinal widths. Since we are interested in electron precipitation, we must be able to distinguish between 5577 Å emissions from precipitating energetic protons and the emissions produced by electrons. Consequently we use the 4861 Å H_{β} emission line to monitor any proton aurora (Fukunishi, 1975).

The intensity of the 5577 Å emission can also be used to determine whether the emissions are caused by energetic protons or by electrons. Under quiet geomagnetic ($K_p < 2^-$) conditions, proton aurora seldom have 5577 Å emissions with intensities greater than several hundred Rayleighs (Wiens and Vallance Jones, 1969). Higher intensity of 5577 Å emission probably indicates an electron precipitation. One final point in helping to determine whether the proton precipitation is present is that the statistical studies show that the center of the proton auroral oval lies a few degrees equatorward of that of the electron oval before midnight and crosses somewhat poleward of it after 1:00 hours geomagnetic time (Wiens and Vallance Jones, 1969).

Following our theoretical analysis in the last chapter, if the shear Alfvén wave mode converts to the kinetic Alfvén wave in the resonant region, the parallel electric field carried by the wave might modulate electron precipitation causing the periodic intensity variations in the optical aurora in the region near the field

line resonance. Therefore, we can examine the period of the arc modulation and the period of the field line oscillations to determine if there is any correlation between the resonant Alfvén wave and optical aurora . The second important physical parameter to measure is the latitudinal phase variation in the modulated optical aurora. Crossing the resonant position, the phase has a 180° latitudinal phase shift (Walker, 1979; 1981). The magnetic fields measured on the ground will have a reversal in the sense of polarization from one side of the resonance to the other. We have measured these parameters in three auroral events, September 28, 1988 (88272), December 8, 1989 (89342), and December 9, 1989 (89343).

3.2.2 Auroral emissions and MPA data

We process the MPA data based on the assumption that an auroral arc consists of thin sheets of luminosity aligned along the geomagnetic field line. The assumption leads to a good approximation for the true horizontal profile if the aurora is nearly overhead, or if the arc is observed by ground based scanning photometers separated by several hundred km distance at both sides of the auroral arc (Romick and Belon, 1966; 1967). In fact, the auroral emission is not a thin sheet of luminosity. It has a width in the north-south direction, which ranges from a few kilometers to 100 km or more for a quiet arc. The optical intensity is an integrated measure for the optical path from the auroral form to the photometer. Therefore, the total optical intensity often can not give details about an emission profile, particularly for arcs near the horizon of the field of view.

In fact, in our project we are concerned with the temporal variation of auroral emissions. This variation of auroral luminosity is produced by a modulation of electron precipitation associated with MHD wave fields. In the resonant Alfvén wave region, the field line resonances have latitudinal changes in the phases of the north-south (and possibly field-aligned) electric fields. If we are to look for these

latitudinal phase changes in the measured variations in the auroral luminosity, then the arc must be near the zenith of the observational field of view. Measurements from arcs away from the zenith will give poor results because the optical path crosses through the entire latitudinal range of the arcs, and the latitudinal changes in phase will not be detected. We determine the phases of the luminosity fluctuations by using the complex demodulation method (see Appendix B).

In our precipitation model, the auroral electrons travel along the geomagnetic field line precipitating into the ionosphere. The average maximum intensity of 6300 \AA occurs at 230 km above the ground and 5577 \AA at 110 km. Even though the red line will be seen south of the green line in geographic coordinates, the red and green will be at the same latitude in geomagnetic coordinates.

3.2.3 The method of data processing

Before any spectral analyses, the time series are detrended to remove linear trends and then high pass filtered with a Butterworth filter. The cut-off frequency is selected at 0.7 mHz . The ULF wave fields we are studying have periods about 250 to 1000 seconds, and consequently we used a 1 hour long window for the time series, giving 0.28 mHz resolution in the frequency domain.

The magnetometer data are processed using the MPE estimator discussed by Samson (1983). This method estimates the pure states in the spectra of the X, Y and Z components from each station. The spectra we show are the total energy of the pure state, and the polarization is computed from the state vector. Here we define the ellipticity as the ratio of the length of the minor axis to the length of the major axis in the horizontal plane. If the ellipticity is negative, the perturbation vector rotates in the clockwise direction, and if positive, in the counterclockwise sense, in respect to the downward view to the ground. Since the field line resonances tend to be highly polarized in a unitary space, the MPE estimator

often gives clearer power spectra than do standard spectral estimators. For the MPA data, we determine the power spectra using discrete Fourier transforms of the time series from each of the 17 bins.

We calculate the phases of the luminosity fluctuations using the complex demodulation method for all 17 bins, assuming a fixed central frequency (see Appendix B). The method has been used to analyse Pi2 pulsation events (Banks, 1975; Beamish, 1979). In our data processing, we use a frequency window with a width of 1.04 mHz and shift the centre frequency, where the maximum power peak occurs, to zero. We then take the inverse FFT transformation after filtering with a low pass Hanning frequency domain filter. The transformed time series give the phase and demodulated amplitude.

Table 3.1: Latitude conversion table for MPA data

Bin No.	Gillam				Rankin			
	5577		6300		5577		6300	
	EDFL ¹	INV. ²	EDFL	INV.	EDFL	INV.	EDFL	INV.
1	68.00	71.20	71.50	74.43	74.50	77.20	78.00	80.28
2	67.50	70.72	70.50	73.70	74.00	76.75	77.00	79.58
3	67.00	70.23	69.50	72.91	73.50	76.33	76.00	78.86
4	66.50	69.33	67.50	72.11	73.00	75.89	75.00	78.11
5	66.00	69.33	67.50	71.26	72.50	75.42	74.00	77.28
6	65.50	68.79	66.50	70.36	72.00	74.97	73.00	76.44
7	65.00	68.31	65.50	69.42	71.50	74.49	72.00	75.55
8	64.50	67.81	64.50	68.44	71.00	74.05	71.00	74.64
9	64.00	67.32	63.50	67.45	70.50	73.58	70.00	73.70
10	63.50	66.83	62.50	66.47	70.00	73.12	69.00	72.77
11	63.00	66.35	61.50	65.49	69.50	72.66	68.00	71.83
12	62.50	65.86	60.50	64.53	69.00	72.19	67.00	70.94
13	62.00	65.36	59.50	63.61	68.50	71.73	66.00	70.06
14	61.50	64.86	58.50	62.71	68.00	71.19	65.00	69.21
15	61.00	64.36	57.50	61.86	67.50	70.79	64.00	68.39
16	60.50	63.88	56.50	61.07	67.00	70.32	63.00	67.61
17	60.00	63.39	55.50	60.33	66.50	69.86	62.00	66.89

¹Eccentric Dipole Field Line Latitude (Cole, 1963), ²Invariant Latitude.

Table 3.2: Location of magnetometer stations

Station	Latitude(N)	Longitude(W)	EDFL Latitude	INV. Latitude
Rankin Inlet	62.49	92.07	70.38	73.54
Eskimo Point	61.06	94.04	68.63	71.77
Fort Churchill	58.44	94.04	66.31	69.57
Back	57.40	94.04	65.18	68.49
Gillam	56.22	94.42	63.87	67.18
Island Lake	53.51	94.40	61.28	64.73
Pinawa	50.09	95.53	57.68	60.95

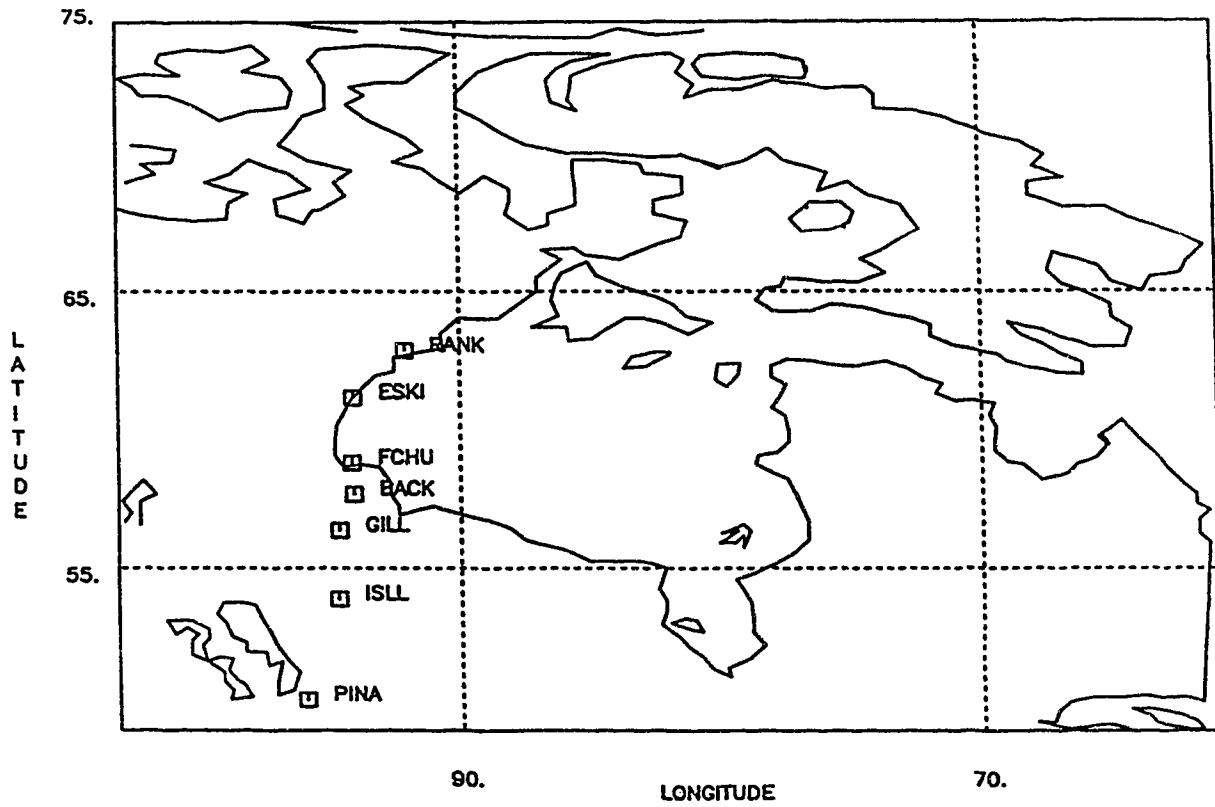


Figure 3.1: CANOPUS system map in geographic coordinates.

Chapter Four

OBSERVATIONS OF AURORAL ARCS AND ASSOCIATED RESONANT ALFVÉN WAVES

4.1 Observations of ULF waves in the magnetometer data

We have analysed the data in three events which include intervals with arcs in the MPA 5577 Å and 6300 Å emissions before midnight. All the events occur before the onset of substorm intensification, and in intervals with low magnetic activity ($Kp < 2^-$).

Figures 4.1 to 4.3 give the X component data for magnetometers near Hudson Bay, on September 28, 1988 (88272), December 8, 1989 (89342), and December 9, 1989 (89343). The local magnetic time is UT minus approximately 6 hours for these magnetometer locations. We can see obvious long period waves between 1:00 to 6:00 UT in event 89342 at Gillam in Figure 4.1 before the onset of a substorm at 6:45 UT. The same magnetic disturbances also occur in events 88272 and 89343 in Figures 4.2 and 4.3.

It is important to realize that the ionospheric conductivity plays a major role in the transmission of the magnetic fields of ULF waves to the ground (Hughes, 1976). In some events, the increase of ionospheric conductivity which is produced by localized auroral particle precipitation can lead to complicated spatial and temporal structures, adding noise and distortions to the magnetic fields that are seen on the ground. We can see the direct evidence in our MPA data which often show a high correlation between regions of 5577 Å emissions and ULF magnetic pulsations. In these events, the Hall conductivity produced by energetic electrons plays a substantial role in determining the morphology of magnetic fields which are detected below the ionosphere by our ground based magnetometers.

4.2 Observations of MPA aurora

In this part, we introduce the MPA data. Figures 4.4 to 4.7 are plots of MPA auroral intensity against time and Invariant latitude for events 88272, 89342 and 89343. In event 88272, there is a small substorm intensification at 4:45 UT (see the Gillam data in Figure 4.4). There is a stable arc which drifts equatorward from 2:00 to 4:00 UT. This arc has green line emissions which are much stronger than the red line emissions. There are no observable H_β emissions so that this arc is likely a pure electron aurora. Event 89343 has a similar arc morphology before the onset of a substorm (Figure 4.7), so it also has a pure electron aurora.

Figures 4.5 and 4.6 show the MPA data at Gillam and Rankin Inlet for event 89342. We think that there are two types of auroral arcs in these data during the interval from 3:30 to 6:30 UT. One is a set of quiet arcs between 69° and 72° Invariant latitude in the 6300 \AA emissions. Other arcs occurring in the event are discrete arcs that appear at higher latitudes from 74° to 80° . The discrete arcs drift slowly equatorward. At Rankin Inlet, the discrete arcs occur near zenith, so we are able to see these arcs distinctly with good latitudinal resolution. However, at Gillam, all of these arcs appear at the northern edge of the field of view. Consequently, the optical paths cross through the entire latitudinal width of the arcs, and the structures are not resolved.

The quiet 5577 \AA emissions occur between 66° and 69° Invariant latitude. Due to the lower latitude location, we only see the stable arc in 5577 \AA emission at Gillam. We also can see stable H_β emission, and its latitudinal location is very close to the position of the 5577 \AA emission. This means that protons are precipitating.

The luminosity of the above three events in 5577 \AA and 6300 \AA emissions is strongly modulated by the resonant Alfvén waves. The modulated amplitude

of oscillation in these emissions is up to 50 percent of their maximum intensity. Figure 4.8 gives an example to illustrate the obvious oscillation in 5577 Å emission for event 88272.

4.3 Data analysis

4.3.1 Event 88272, 3:00-4:00 UT

In analysing event 88272, we selected the interval from 3:00 to 4:00 UT, which is before the time of the substorm intensification. Figure 4.9 shows the pure state power and ellipticity in the magnetometer data. Unfortunately, these data were obtained before the CANOPUS system was fully operational and only four magnetometers were operating. Figure 4.10 shows the power and ellipticity as a function of latitude for the 1.1 mHz pulsation. The cross over in the ellipticity, from negative at low latitudes, to positive at high latitudes, indicates the position of the resonance. The ellipticity is near zero at about 69° and the pure state power is maximum at the same location (between Back and Fort Churchill).

Figures 4.11 and 4.12 are the power spectra of the MPA 5577 Å and 6300 Å emissions observed at Gillam. The largest spectral peak (see bin 5 in the 6300 Å and 5577 Å data) is near 1.3 mHz , agreeing with the results from the magnetometer data. In Figure 4.13, the latitudinal position of the peak power of the 1.3 mHz , 5577 Å emission is near 69° Invariant latitude in accordance with the maximum power of the magnetometer data. In Figure 4.14, the maximum power of the 1.3 mHz , 6300 Å emission is located at 71.3° Invariant latitude. From the analysis of event 88272, we see that the peak power of the 1.3 mHz , 5577 Å, corresponding to the most energetic electrons, coincides with the maximum power in the magnetometer data, and the possible position of the resonance (the latitude with an ellipticity of zero in Figure 4.10).

4.3.2 Event 89342, 5:00-6:00 UT

The substorm intensification in event 89342 has been systematically studied by Samson (1991c). Here we look at the modulated particle precipitation before the onset of the intensification (5:00 to 6:00 UT). The 4861 Å emission (in Figure 4.5) indicates that there is considerable proton precipitation near the zenith at Gillam.

Inspecting Figure 4.15, we can see that the peak power of the magnetic pulsation is at about 1.39 mHz. Figure 4.16 is a plot of the power and ellipticity against Invariant latitude. The ellipticity varies in a complex form that may not be accurate at Island Lake and Rankin Inlet, as the spectra have strong power at cut-off frequency of 0.7 mHz. The field line resonance may be near 67° as there is a maximum in the power and a change in ellipticity there.

Figure 4.17 shows the power and phase for 5577 Å and 6300 Å emissions at Gillam. There are mainly two maxima in the 5577 Å emissions. The first at 70° Invariant latitude has a smooth latitudinal phase shift. The second peak, occurring at 67.8°, is accompanied by electron precipitation modulated by resonant waves. Its position corresponds to the zero ellipticity in Figure 4.16. H_{β} occurring at this latitudinal position indicates that some protons also precipitate into the region. In checking 6300 Å emissions, we find that there are also two peaks in 6300 Å emission at Gillam. The maximum power occurs at the higher latitude where some strong discrete arcs exist. We can see smooth phase shift at these latitude ranges. This is perhaps due to the integrating effect along the optical path. The second maximum occurs near 69° Invariant latitude, possibly in association with the resonance.

In comparing Figures 4.16 with 4.17, we can make the following summary. The zero in the ellipticity (Figure 4.16) lying near 67.7° Invariant latitude is

associated with the energetic electron precipitation seen as 5577 Å emissions. There is second zero ellipticity at the higher latitude in event 89342. Near this position, optical emissions in 5577 Å and 6300 Å emissions have strong power with increasing phase change toward to high latitudes.

4.3.3 Event 89343, 4:00-5:00 UT

An inspection of Figure 4.18 (event 89343) clearly indicates the existence of a strong spectral peak, which may be connected to a field line resonance in the evening sector of the magnetosphere. The maximum power of the pure state spectra is at a frequency of about 1.1 mHz in the data from all six magnetometer stations.

Figure 4.19 shows a latitudinal plot of the power and ellipticity at 1.1 mHz (resolution 0.28 mHz). The ellipticity is -0.7 at Island Lake, increasing to $+0.3$ at Eskimo Point, crossing the zero point at 70.3° Invariant latitude. The clockwise polarization of the wave changes to counterclockwise polarization with increasing latitude. At Rankin the ellipticity is negative giving a second zero point at 72.7° Invariant latitude. A comparison of the position of the maximum power with the change in the sign of the ellipticity suggests the resonant Alfvén waves were located at $70^\circ - 72^\circ$ Invariant latitude.

Figures 4.20 to 4.22 show contour plots of the power spectra of the MPA data for Rankin Inlet (5577 Å, 6300 Å) and Gillam (6300 Å), as well as plots of the phase at 1.31 mHz . In comparing the power spectra of the MPA data in Figure 4.20 with the ellipticity of the magnetometer data in Figure 4.19, we find that the latitudinal position of the maximum modulated luminosity power of the 5577 Å emission is very close to the position of the maximum power in the magnetometer data.

Besides the maximum in the power spectrum, the second important feature of field line resonance in the ionosphere is a 180° phase shift crossing the resonance position (Walker, 1979). In our analysis, we find a similar phase shift structure in the MPA data near of the resonant region in a 2° to 4° latitude range. In Figure 4.20, the phase has a 180° shift between 70° to 72° latitudinal band that corresponds to the counter clockwise polarization of magnetometer data in Figure 4.19. The phase has a local minimum at 72° decreasing by about 180° from 70° to 72° , then increasing by about 180° from 72° to 73° . This latitudinal structure in the phase was also seen in event 88272. We will show later that these two 180° phase shifts are related to the propagation and coupling of compressional MHD waves to shear Alfvén resonances.

Year:1988 Day:272 X
Start Time 1988/09/28 00:00:00 UT
Despiked ($\Delta=100$) BETA Data

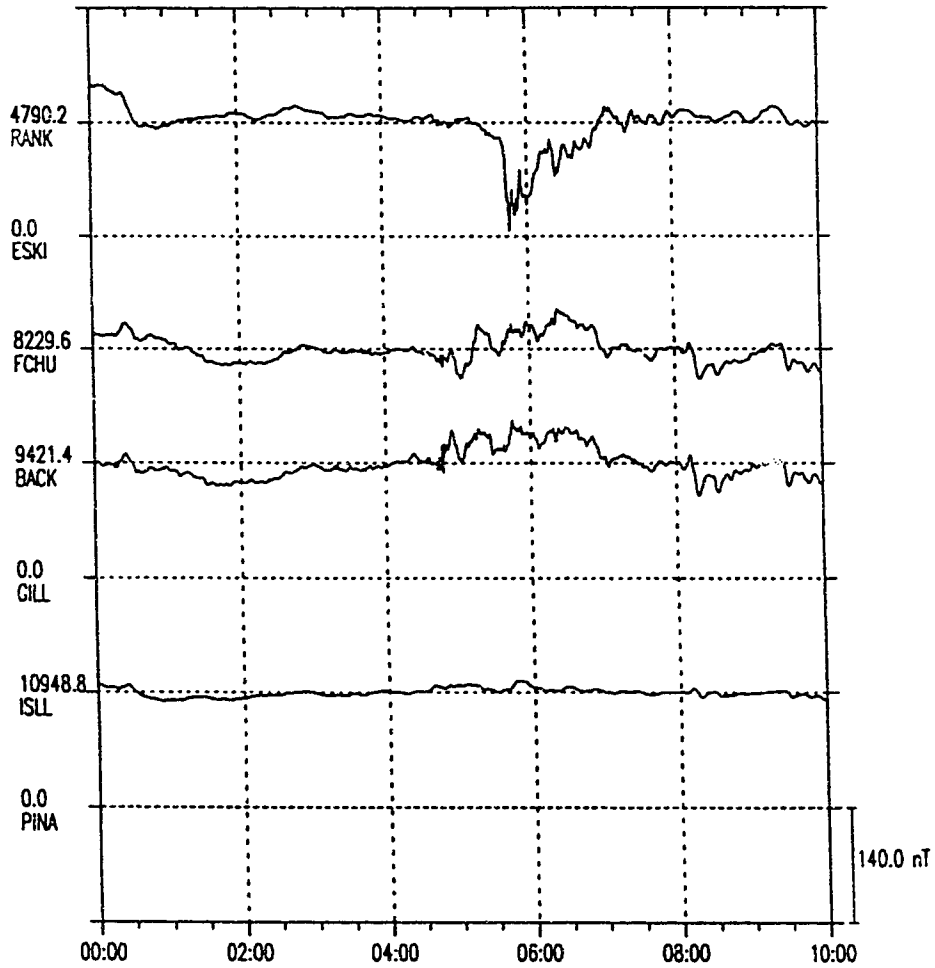


Figure 4.1: X-component of magnetometer data recorded by the eastern line of the CANOPUS system on September 28, 1988

Year:1989 Day:342 X
Start Time 1989/12/08 00:00:00 UT

Despiked ($\Delta=100$) BETA Data

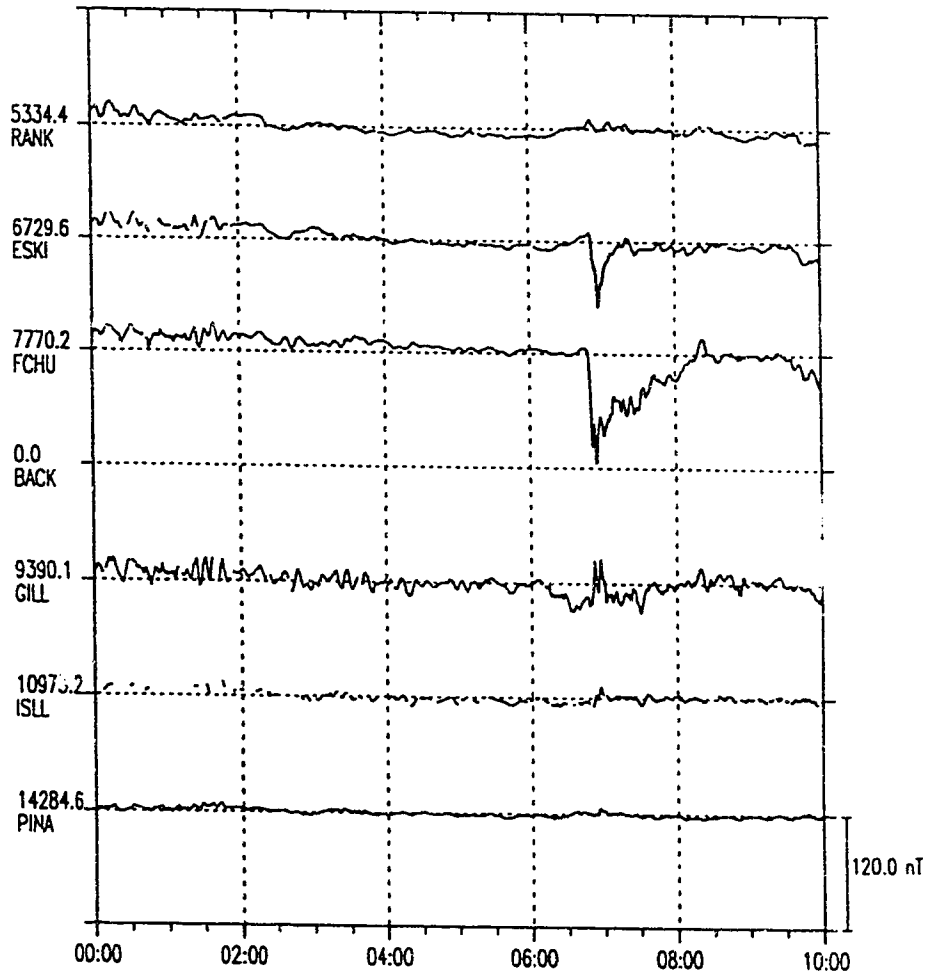


Figure 4.2: X-component of magnetometer data recorded by the eastern line of the CANOPUS system on December 8, 1989

Year:1989 Day:343 X
Start Time 1989/12/09 00:00:00 UT

Despiked ($\Delta=100$) BETA Data

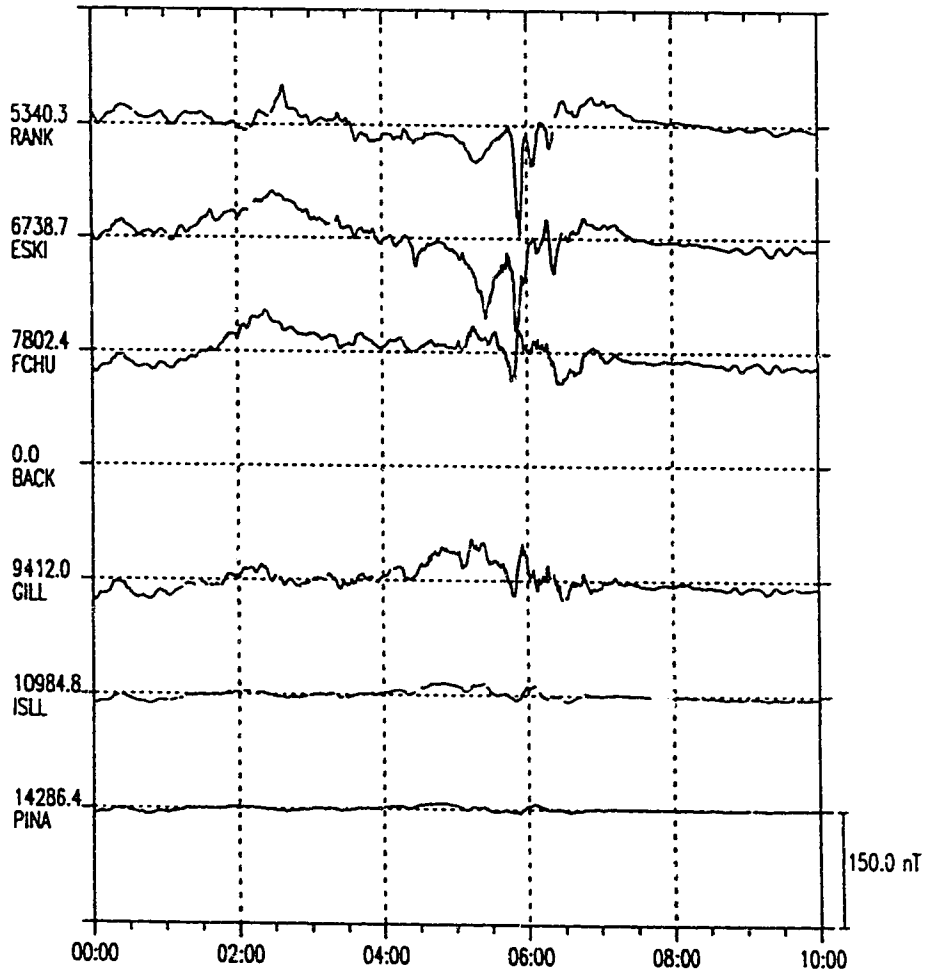


Figure 4.3: X-component of magnetometer data recorded by the eastern line of the CANOPUS system on December 9, 1989

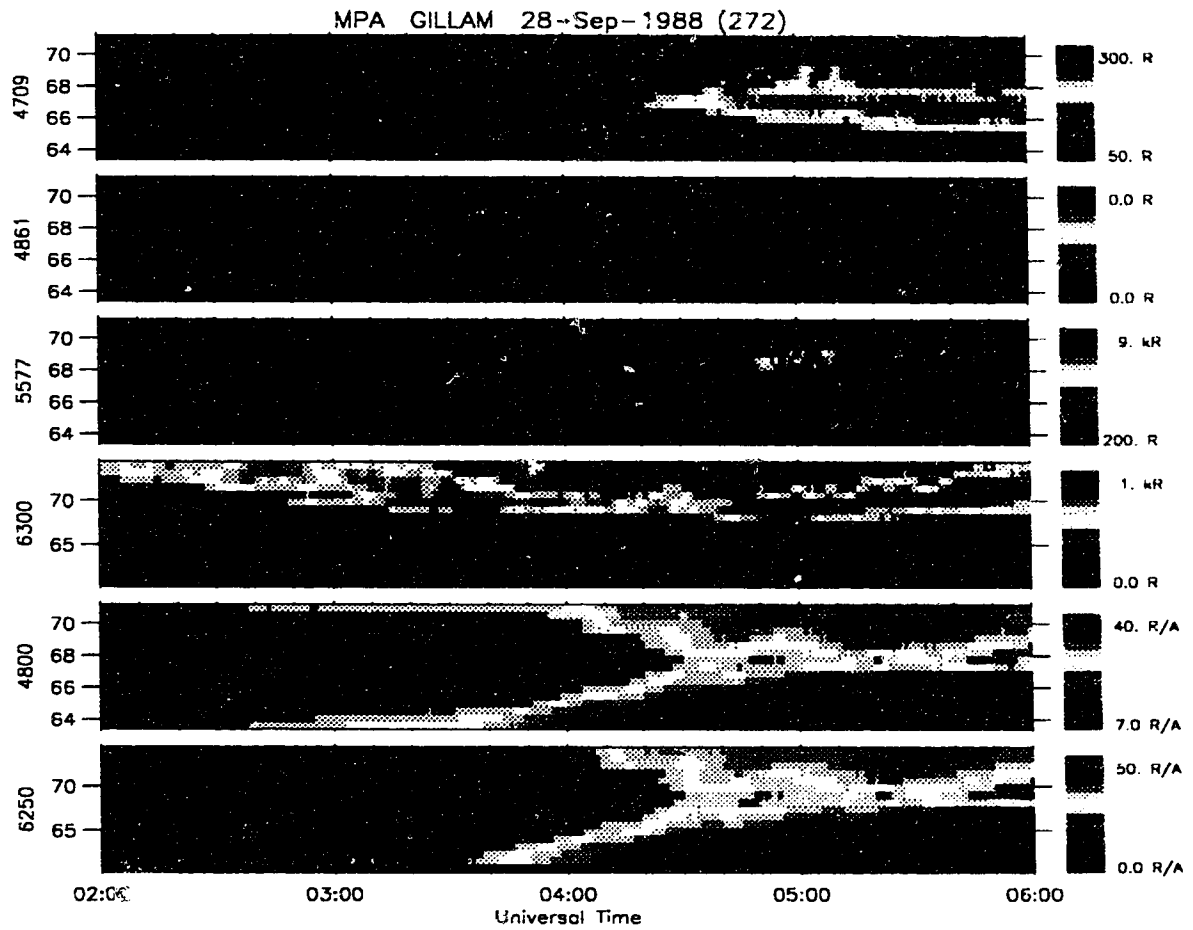


Figure 4.4: Auroral intensity of MPA data against time and Invariant latitude for event 88272 at Gillam station. The color scale is logarithmic in the plot.

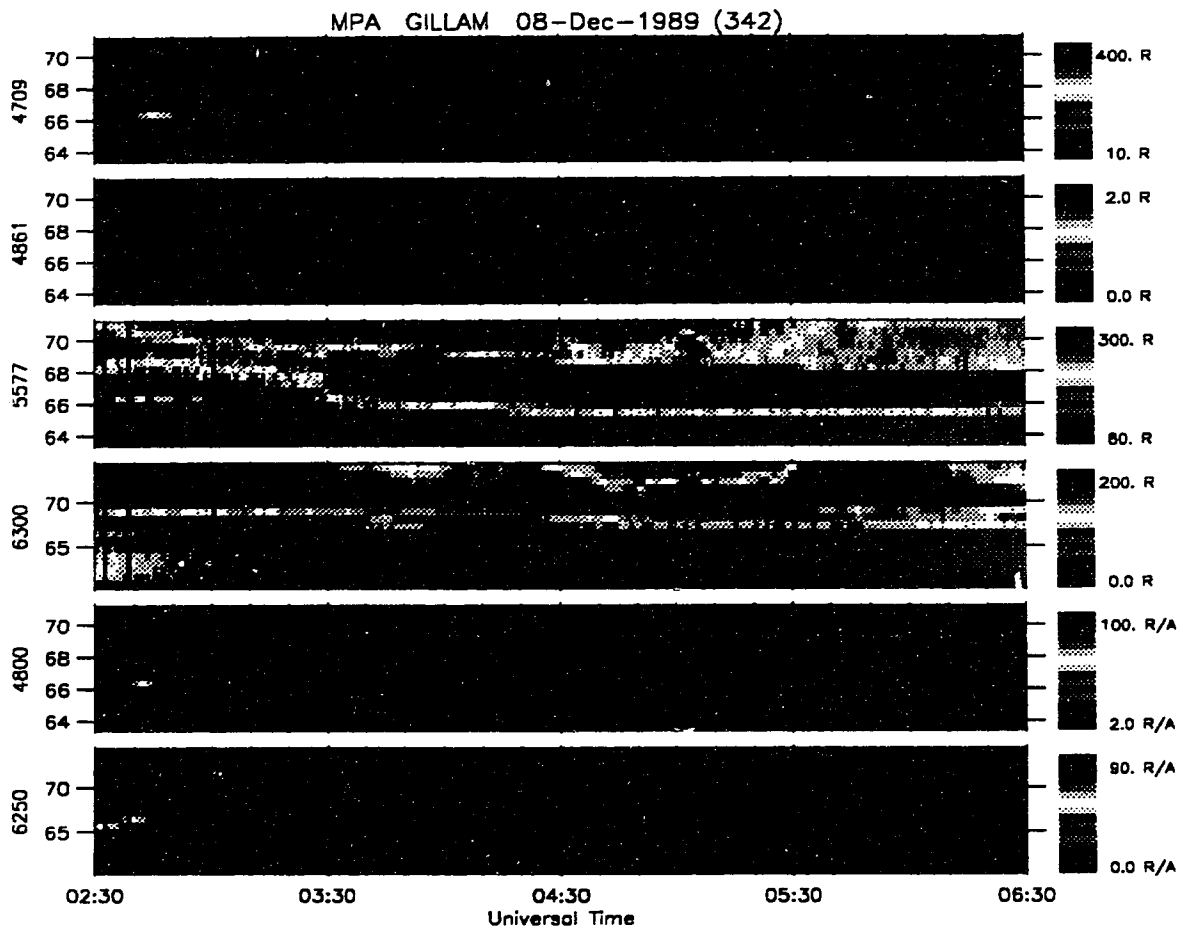


Figure 4.5: Auroral intensity of MPA data against time and Invariant latitude for event 89342 at Gillam station. The color scale is logarithmic in the plot.

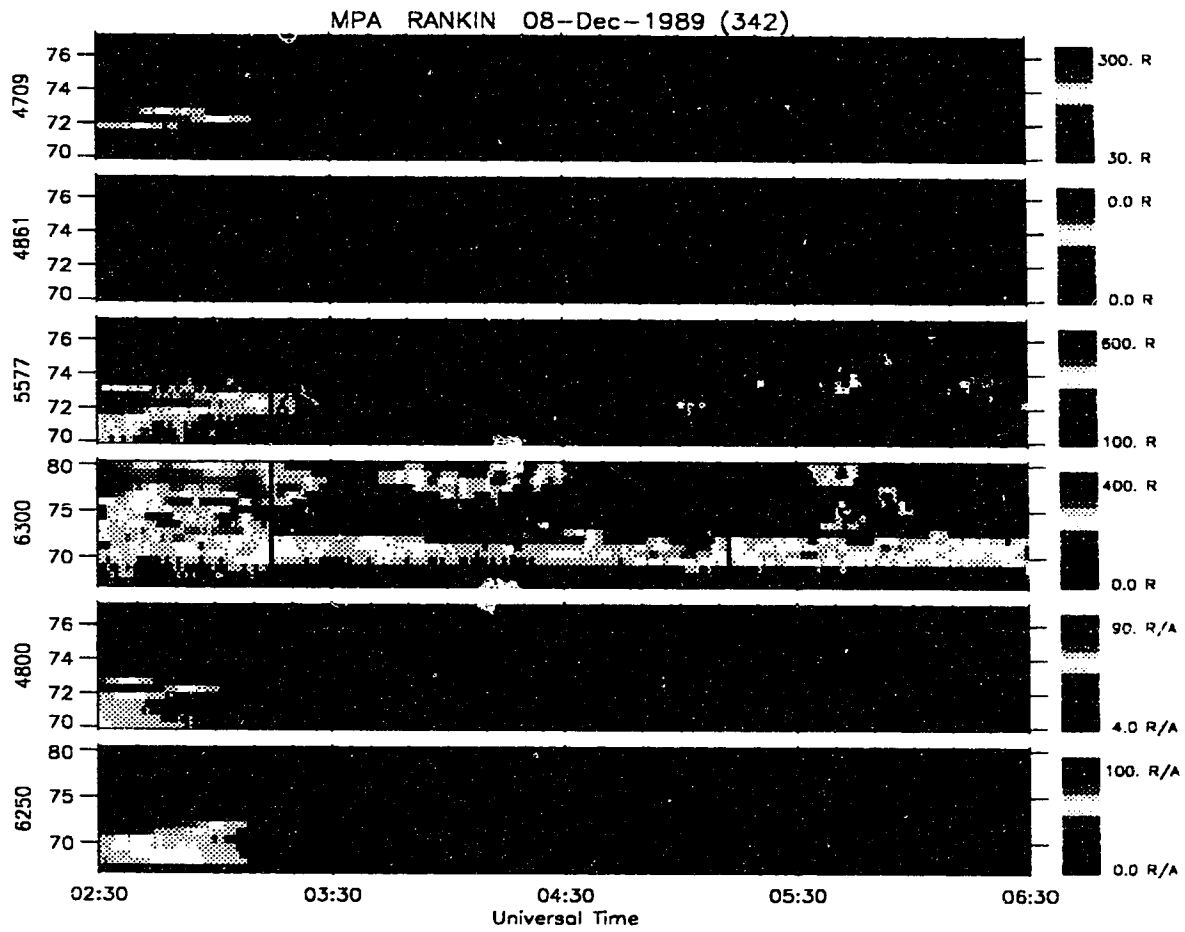


Figure 4.6: Auroral intensity of MPA data against time and invariant latitude for event 89342 at Rankin Inlet station. The color scale is logarithmic in the plot.

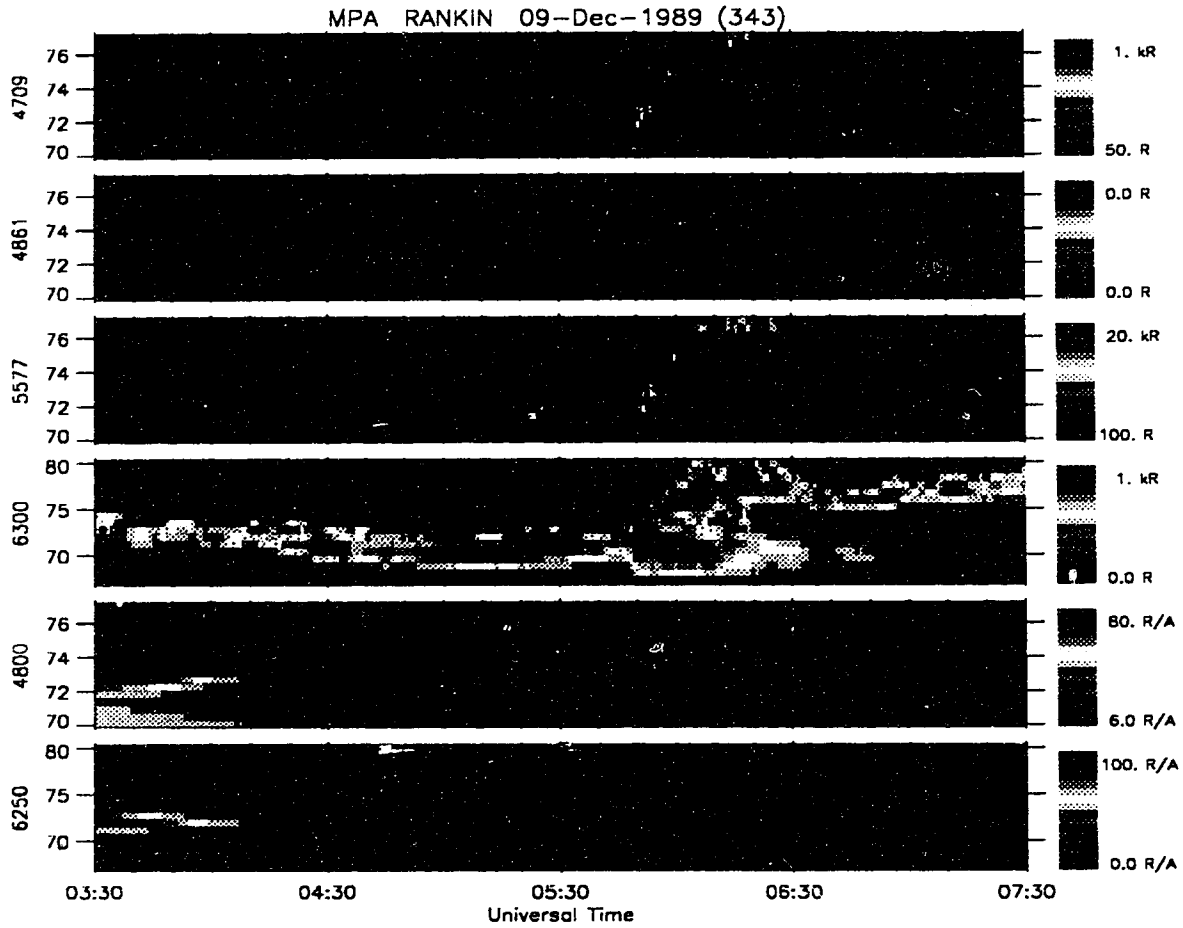


Figure 4.7: Auroral intensity of MPA data against time and invariant latitude for event 89343 at Rankin Inlet station. The color scale is logarithmic in the plot.

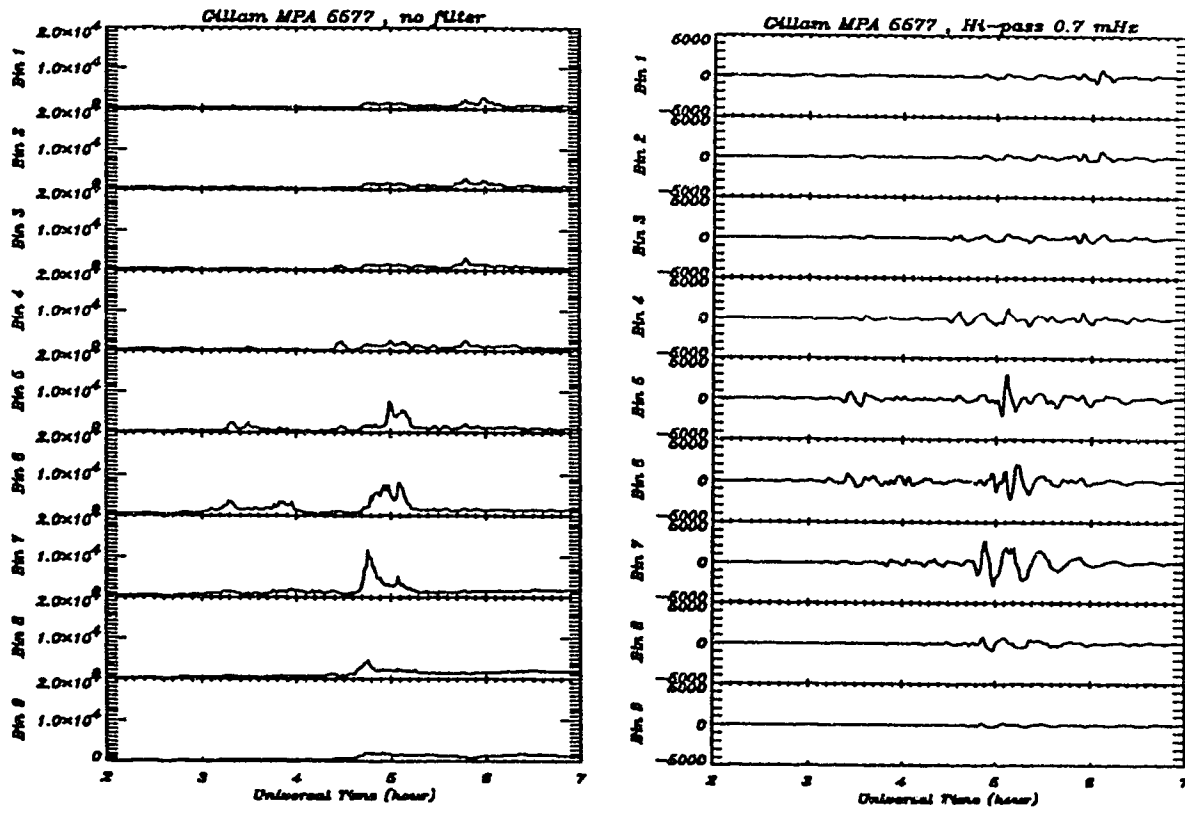


Figure 4.8: (a) Left: Time series of auroral intensity before using hi-pass filter for event 88272. (b) Right: Time series of modulated amplitude of auroral intensity after using 0.7 *mHz* hi-pass filter. The modulated intensity is close to half of the original optical emission intensity.

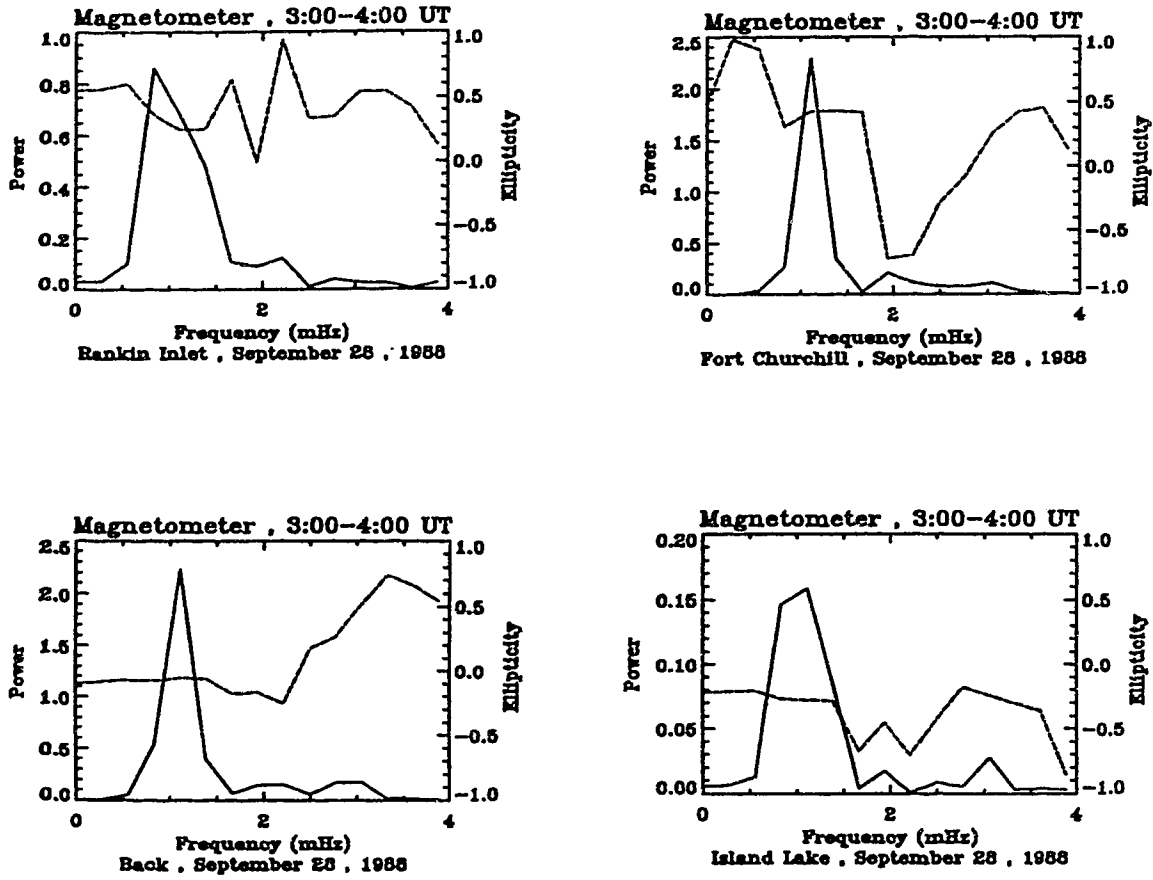


Figure 4.9: Pure state power spectrum for the X+Y+Z components and ellipticity on the X-Y plane in the interval from 3:00 to 4:00 UT, observed by magnetometers of the eastern line stations on September 28, 1988. The data were detrended with a 0.7 mHz high pass filter. The solid line is power (in arbitrary units), and the dashed line is ellipticity.

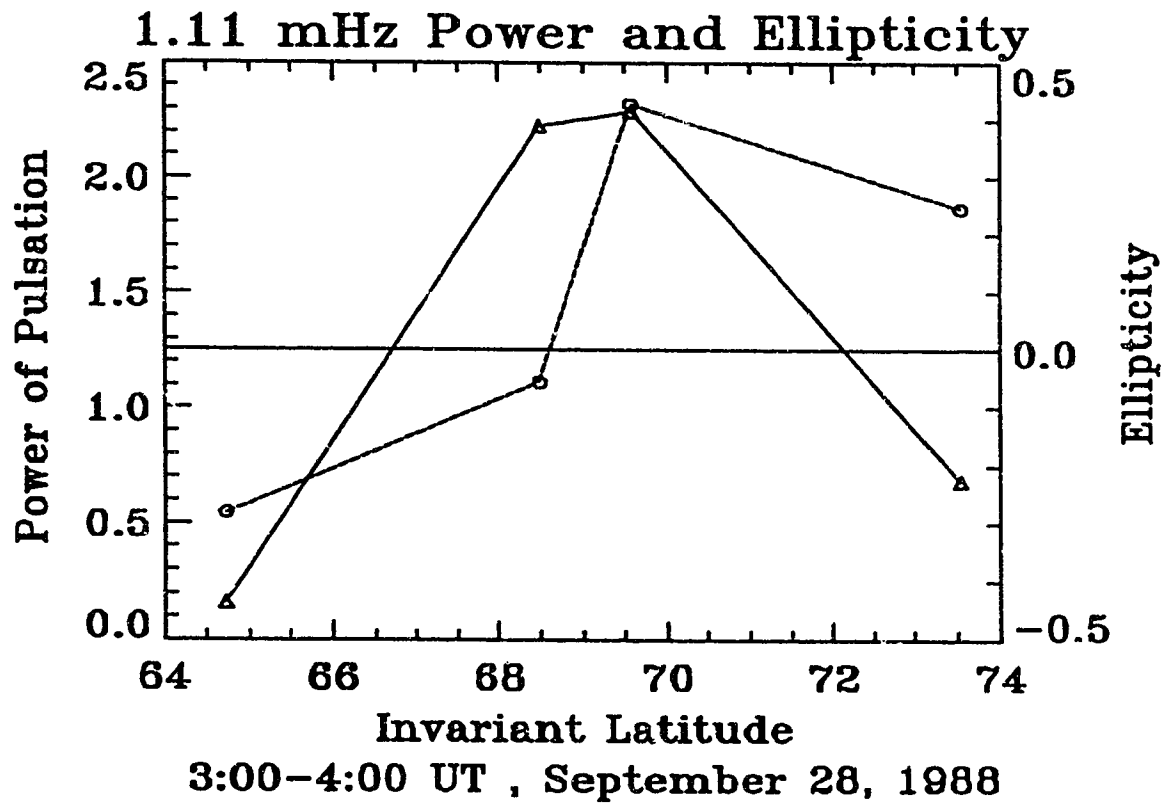


Figure 4.10: Pure state power and ellipticity for 4 stations with frequency equal to 1.11 mHz for event 88272. The dashed line is ellipticity, and the solid line is power.

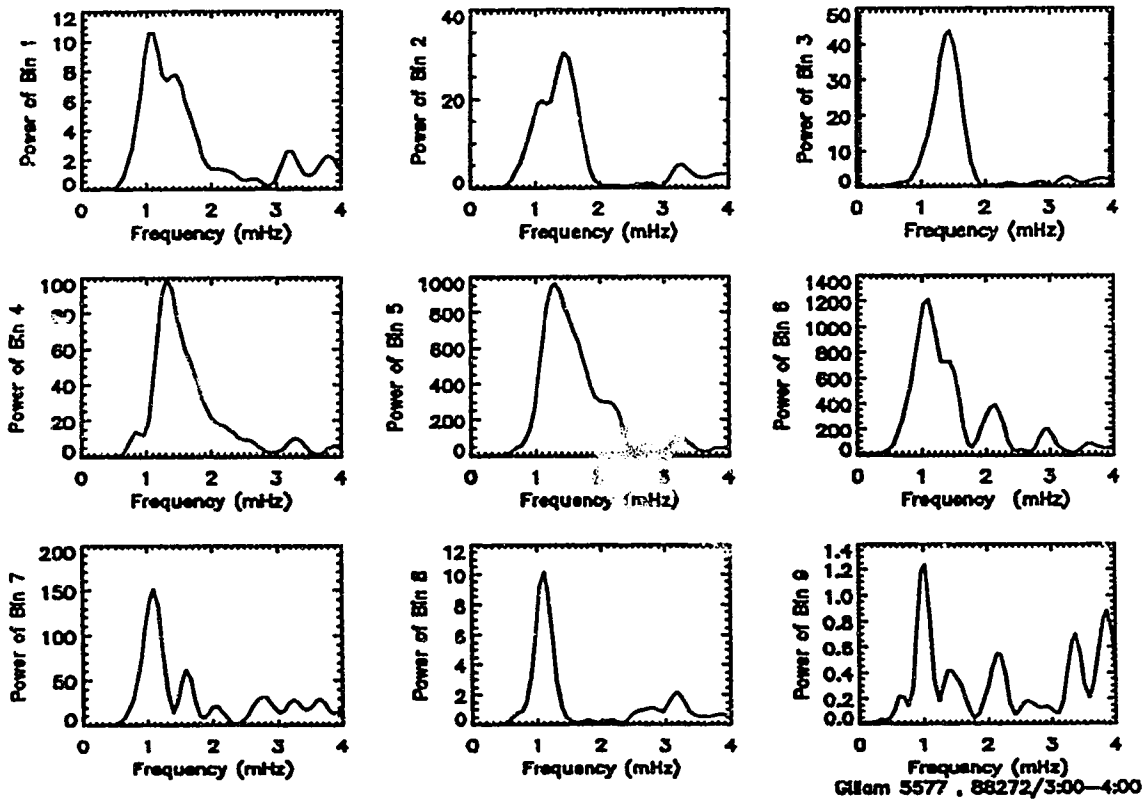


Figure 4.11: Power spectra of MPA 5577 Å emissions observed at Gillam station for event 88272. In the figure, every plot has a different scale. The 0.7 mHz high-pass filter is used.

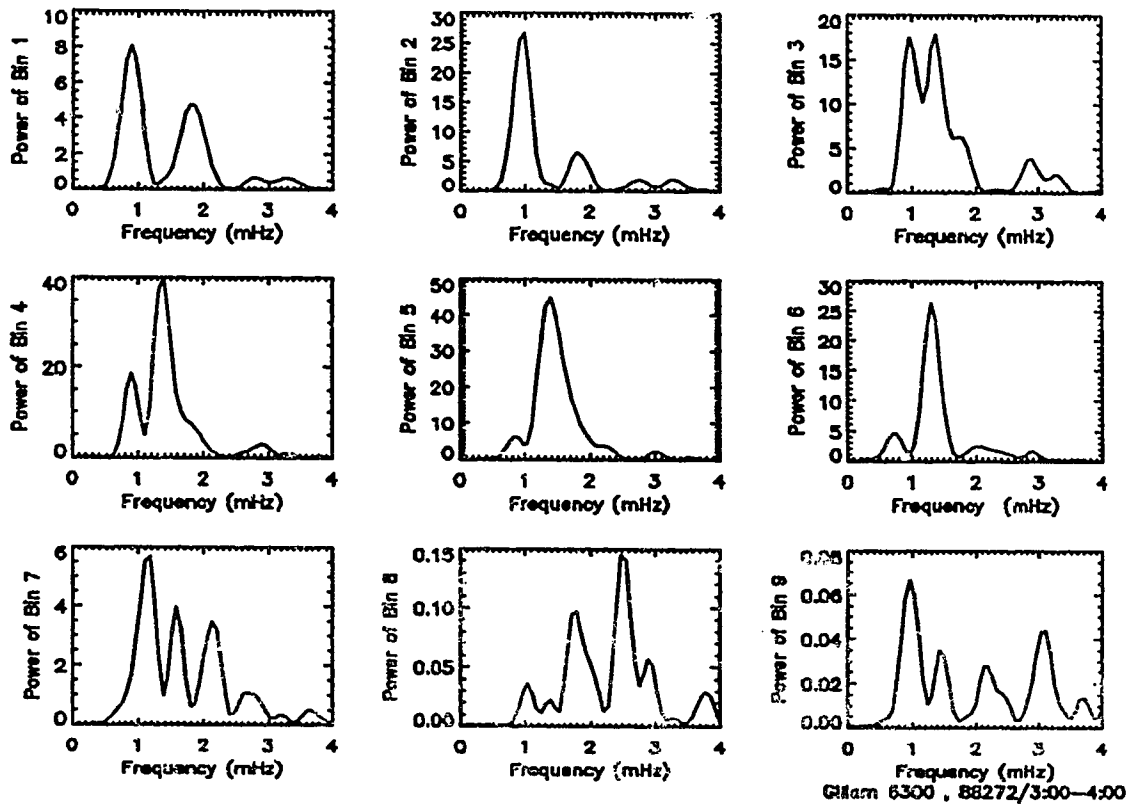


Figure 4.12: Power spectra of MPA 6300 Å emissions observed at Gillam station for event 88272. In the figure, every plot has a different scale. The 0.7 mHz high-pass filter is used.

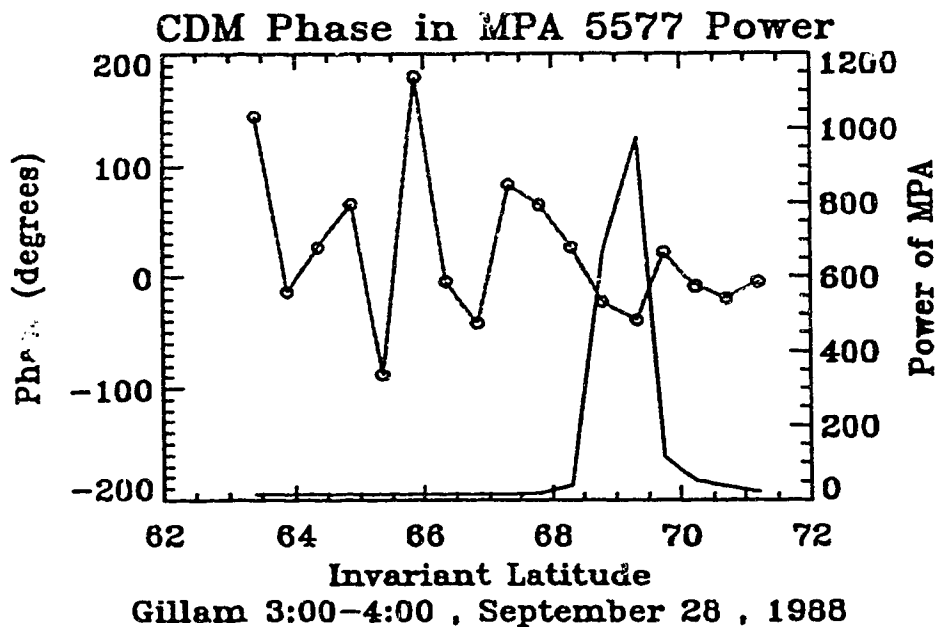
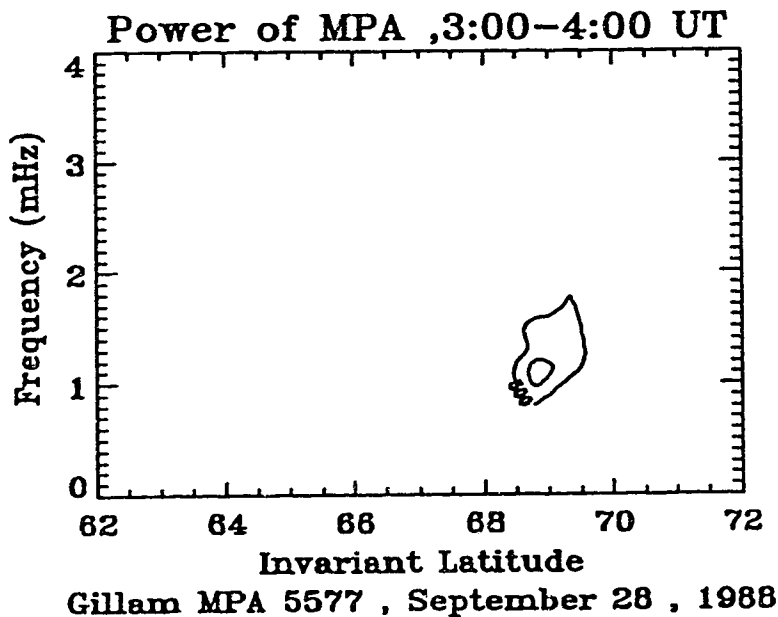
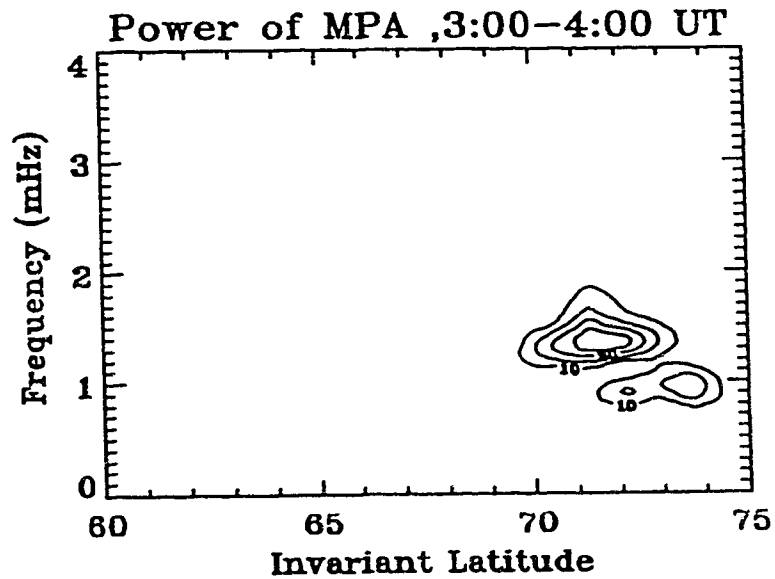
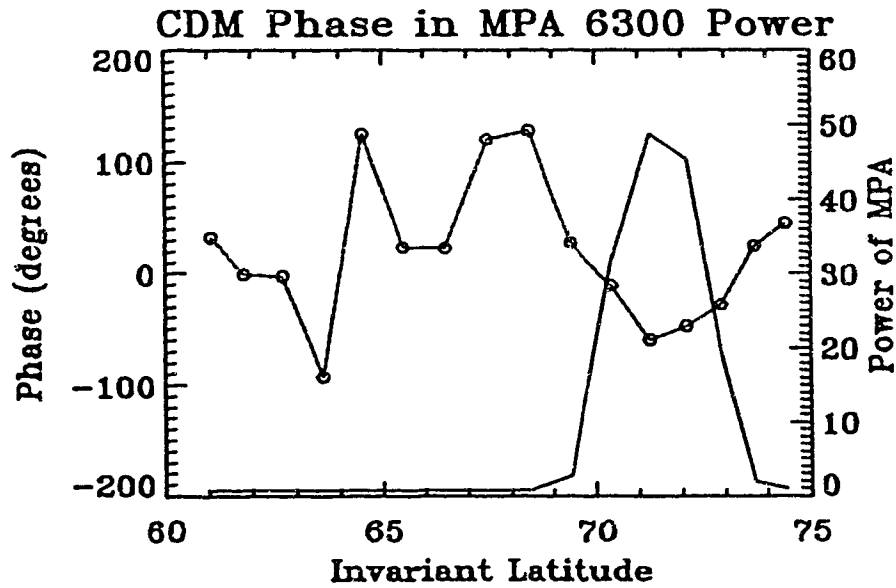


Figure 4.13: (a) Top: Contour plot of MPA power (arbitrary units) of the 5577 Å emissions for event 88272 at Gillam station. (b) bottom: Phase of the 5577 Å emissions with central frequency 1.31 mHz. The dashed line is phase, and the solid line is power plotted against Invariant latitude .



Gillam MPA 6300 , September 28 , 1988



Gillam 3:00-4:00 , September 28 , 1988

Figure 4.14: (a) Top: Contour plot of MPA power (arbitrary units) of the 6300 Å emissions for event 88272 at Gillam station. (b) bottom: Phase of the 6300 Å emissions with central frequency 1.39 mHz. The dashed line is phase, and the solid line is power plotted against Invariant latitude .

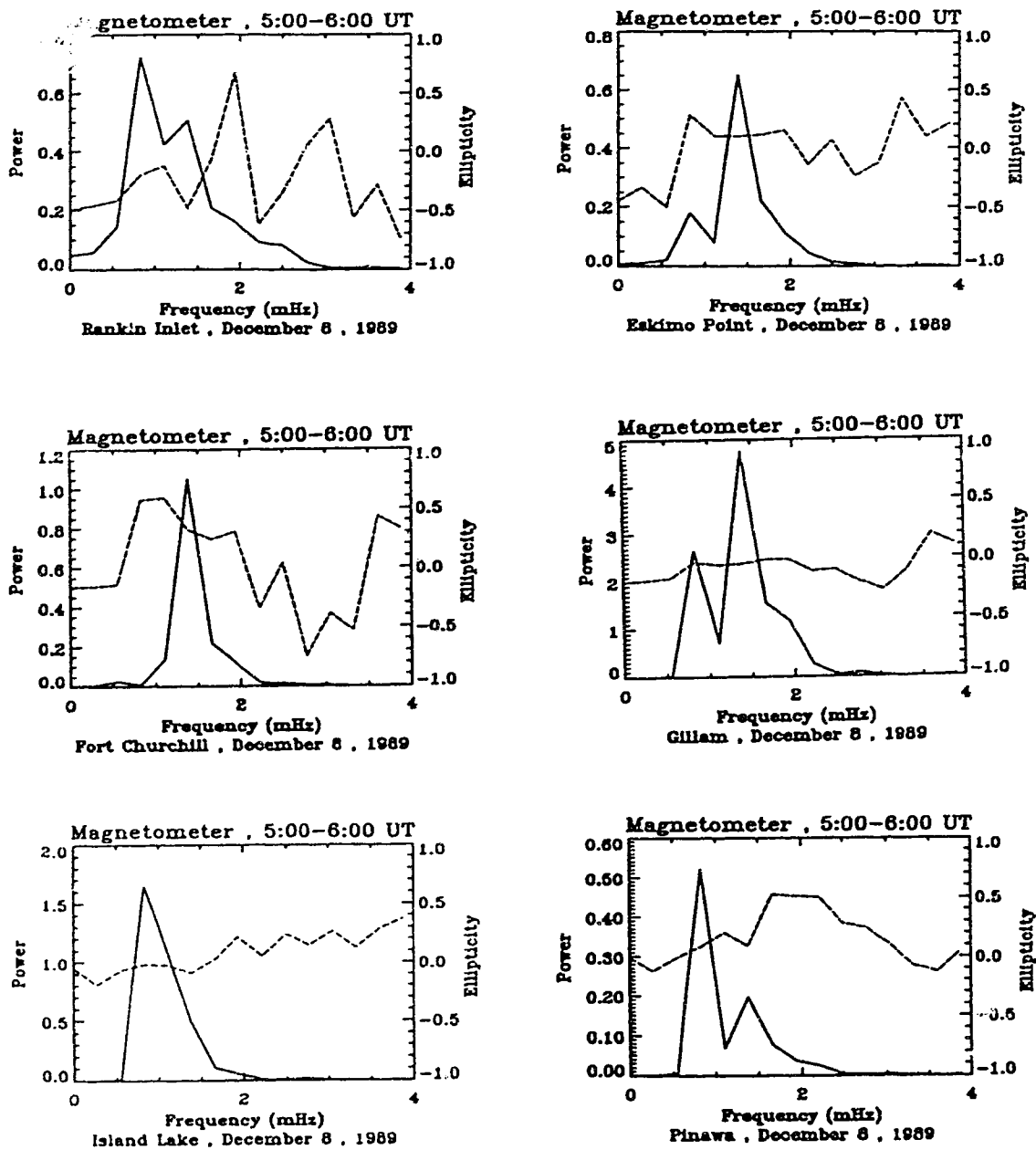


Figure 4.15: Pure state power spectrum for the X+Y+Z components and ellipticity on the X-Y plane in the interval from 5:00-6:00 UT, observed by magnetometer of the eastern line stations on December 8, 1989. The solid lines are power, and the dashed lines are ellipticity.

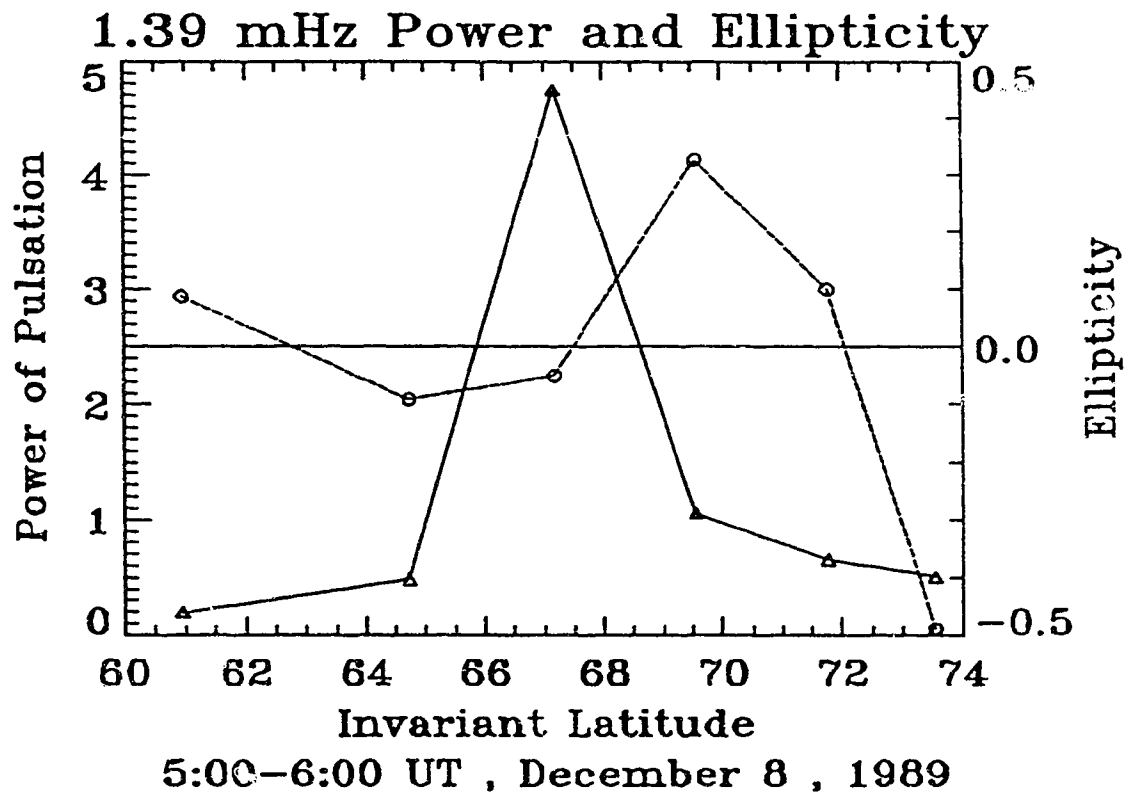


Figure 4.16: Pure state power and ellipticity for 6 stations for pulsations with frequency equal to 1.39 mHz for event 89342. The solid line is power, and the dashed line is ellipticity.

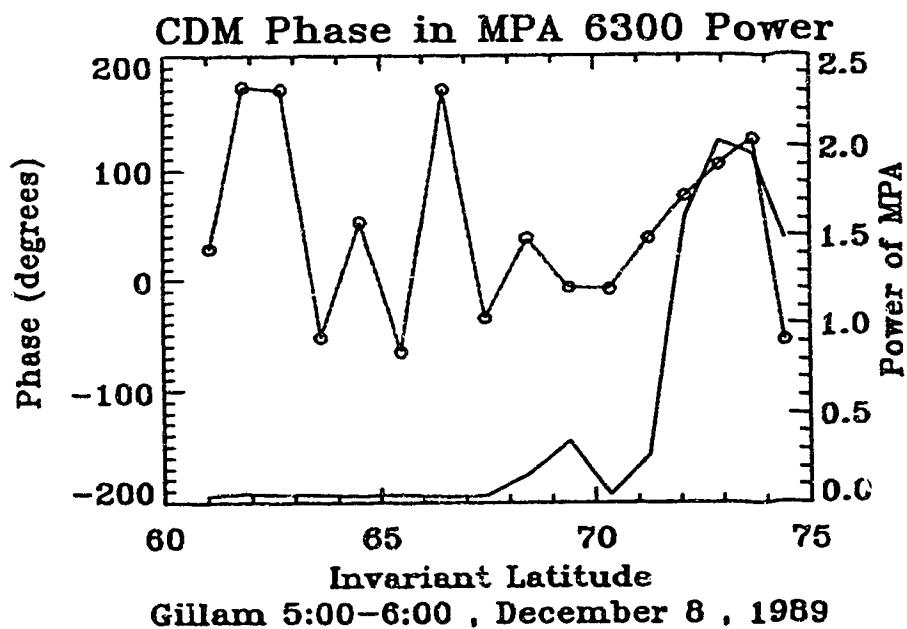
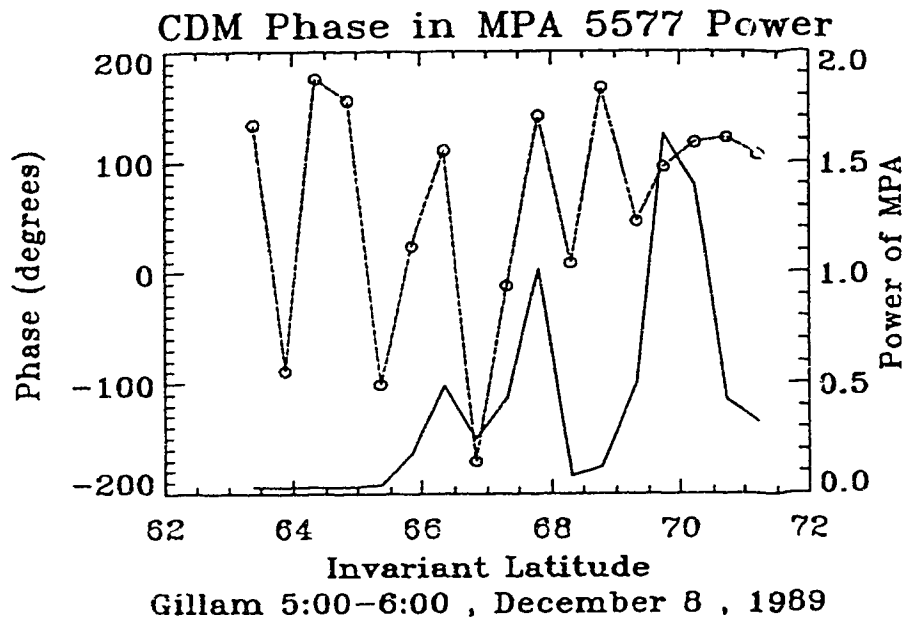


Figure 4.17: (a) Top: MPA power and phase of the 5577 Å emission for event 89342 at Gillam station. (b) Bottom: Power and Phase of the 6300 Å emissions. In data processing, the central frequency is at 1.39 mHz , and the width of frequency window is 1.04 mHz . The dashed line is phase, and the solid line is power plotted against Invariant latitude.

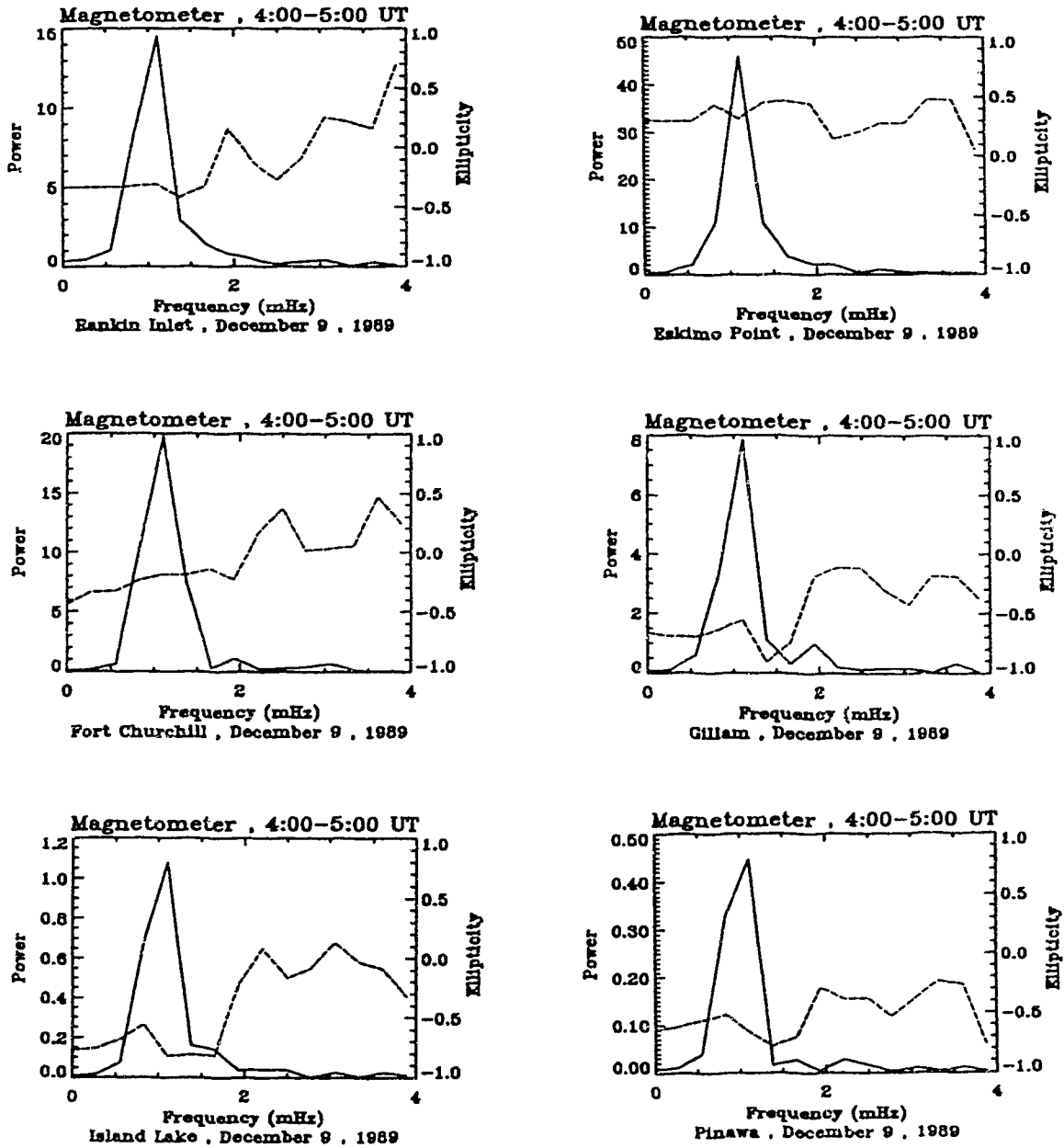


Figure 4.18: Pure state power spectrum for the X+Y+Z components and ellipticity on the X-Y plane in the interval from 4:00-5:00 UT, observed by magnetometers of the eastern line stations on December 9, 1989. The solid lines are power, and the dashed lines are ellipticity.

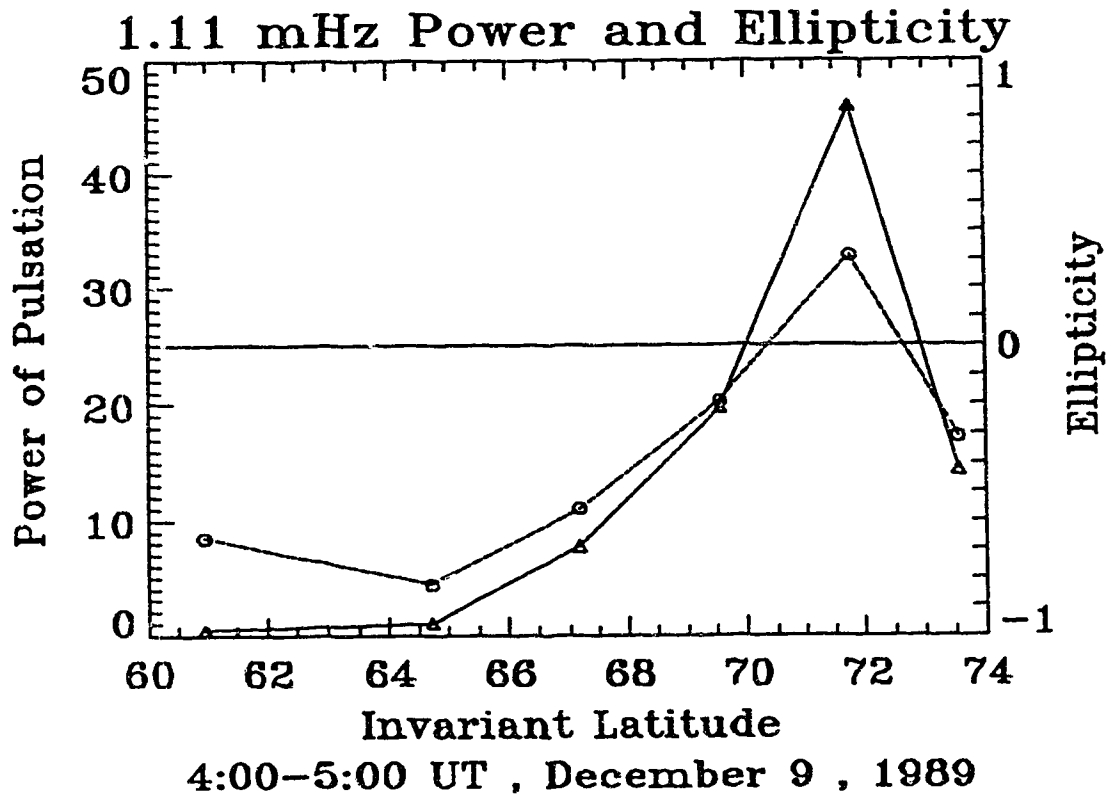


Figure 4.19: Pure state power and ellipticity for the eastern stations , for pulsations with frequency equal to 1.11 *mHz* for event 89343. The solid line is power, and the dashed line is ellipticity.

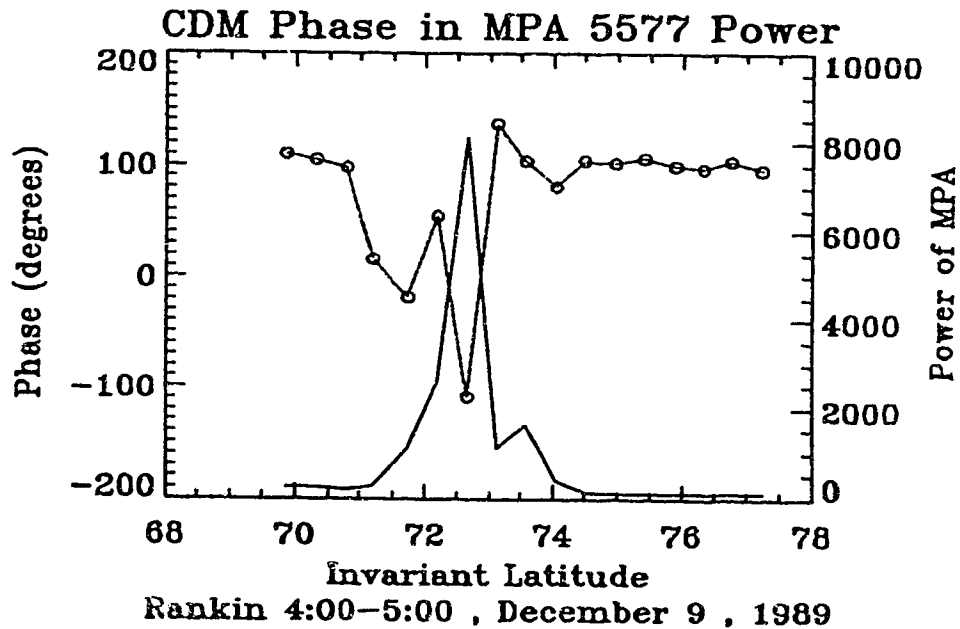
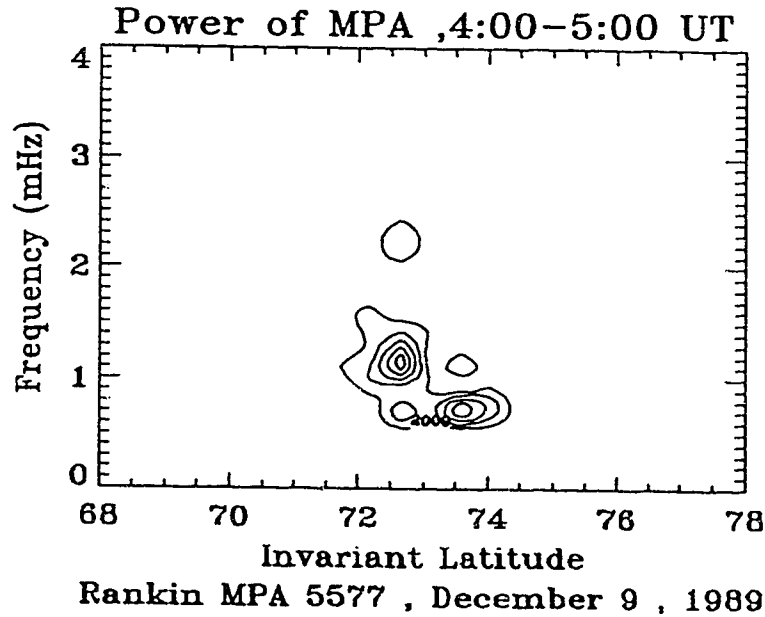


Figure 4.20: (a) Top: Contour plot of MPA power (arbitrary units) of the 5577 Å emissions for event 89343 at Rankin station. (b) bottom: Phase of the 5577 Å emissions with central frequency $\nu = 0.5$ mHz. The dashed line is phase, and the solid line is power plotted against Invariant Latitude.

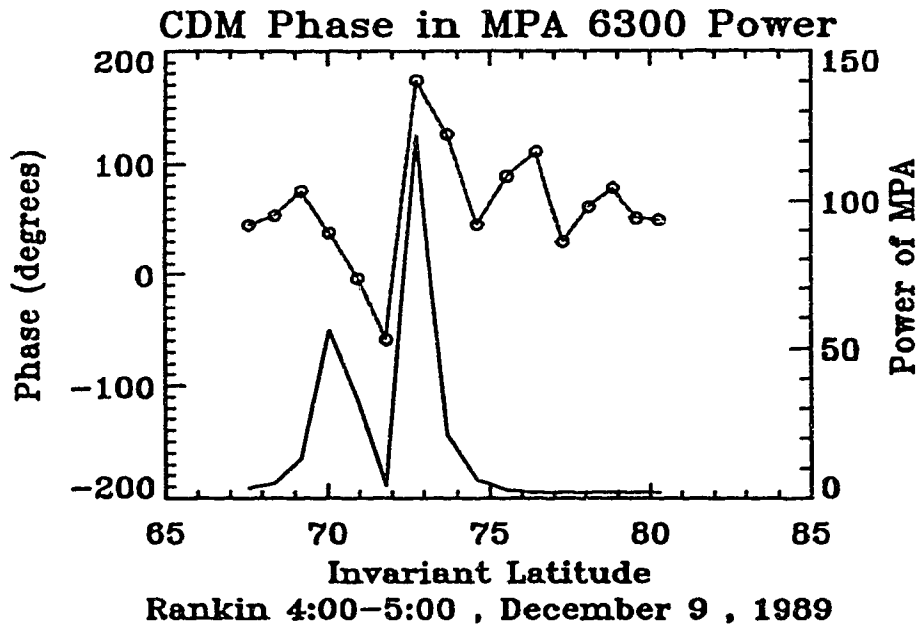
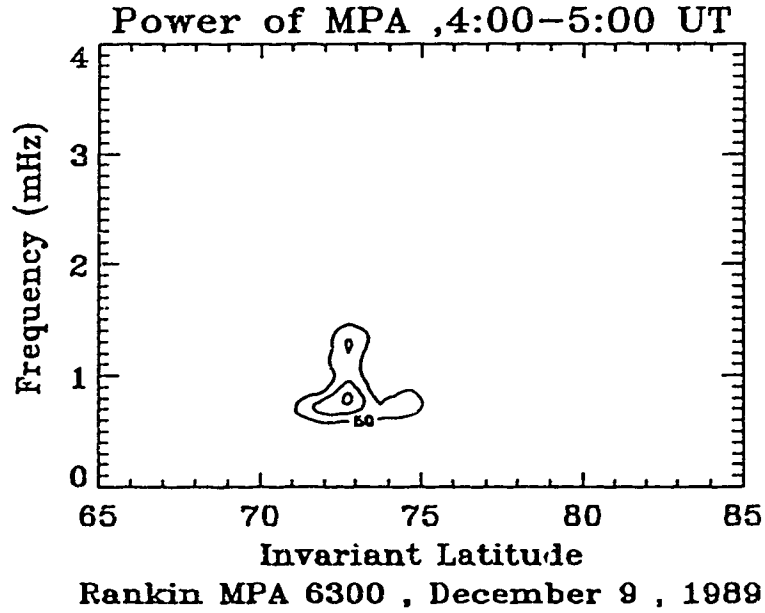


Figure 4.21: (a) Top: Contour plot of MPA power (arbitrary units) of the 6300 Å emissions for event 89343 at Rankin station. (b) bottom: Phase of the 6300 Å emissions with central frequency 1.31 mHz. The dashed line is phase, and the solid line is power plotted against Invariant latitude .

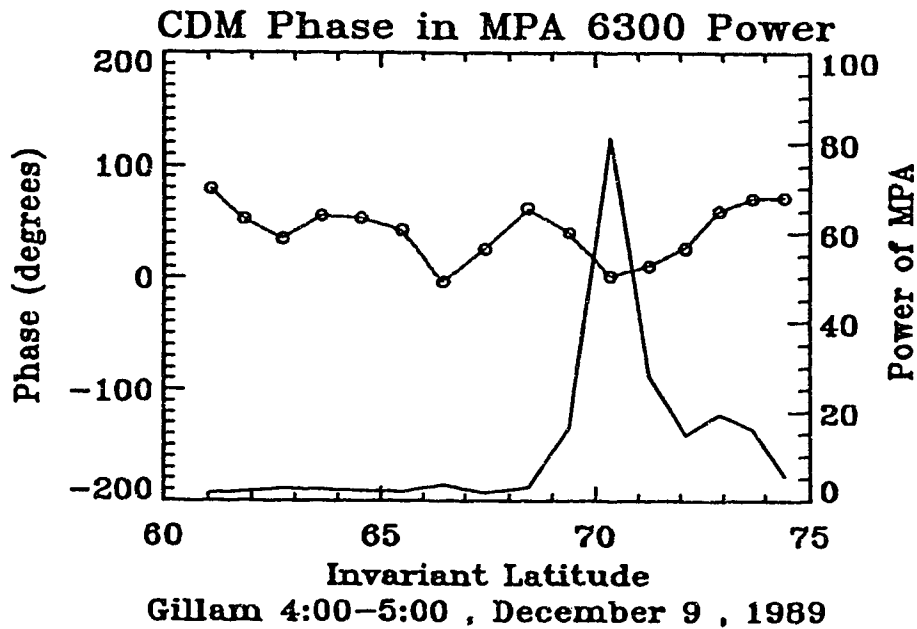
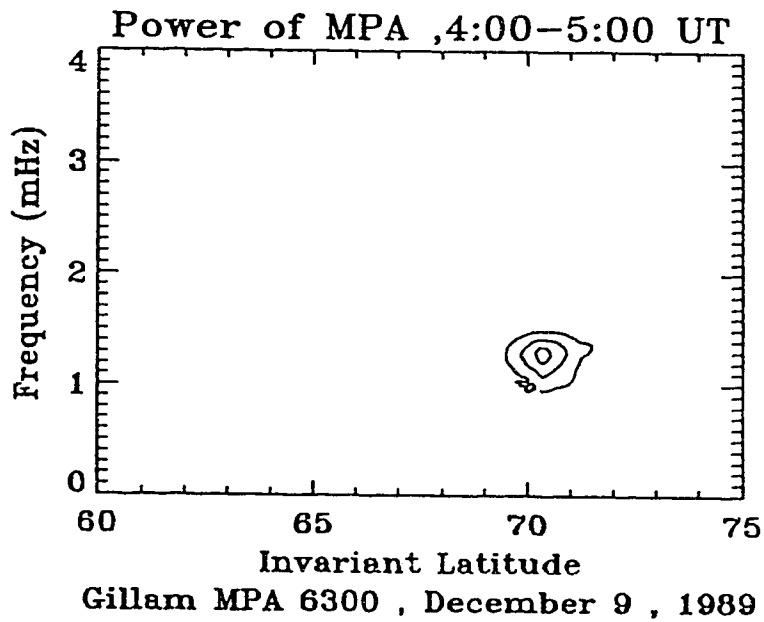


Figure 4.22: (a) Top: Contour plot of MPA power (arbitrary units) of the 6300 Å emissions for event 89343 at Gillam station. (b) bottom: Phase of the 6300 Å emissions with central frequency 1.31 mHz. The dashed line is phase, and the solid line is power plotted against Invariant latitude .

Chapter Five

DISCUSSION AND CONCLUSIONS

5.1 The resonance seen in the magnetometer data

An important experimental result in our comparison of the resonant Alfvén waves observed on the ground by the magnetometer with the ionospheric emissions by the MPA array is that the zero ellipticity of the resonant Alfvén wave in the magnetometer data corresponds to the maximum power of the 5577 Å emissions, and the energetic electron precipitation. We have strong observational evidence to support this point in our study of the modulated 5577 Å emissions in the three events. The latitudinal band bounded by the zero ellipticity points covers the quiet stable arcs seen in Figures 4.4 to 4.7. In this latitude range, the resonant Alfvén wave has counter-clockwise (positive) ellipticity corresponding to the resonant Alfvén wave region from the turning point (northernmost zero) to the resonance (southernmost). This indicates that resonant shear Alfvén wave may cause electron precipitation in pre-substorm, quiet arcs.

In order to analyze the polarization ellipse of the resonant Alfvén wave, we derive a wave polarization parameter called the polarization ratio and given by ξ_y/ξ_x . In Figure 5.1 the amplitude of the argument gives the relative amplitudes of the components of the wave. If the amplitude is very large, the wave is linearly polarized in the ξ_y direction. If the amplitude is near zero, the wave is polarized in the ξ_x direction. A negative sense indicates clockwise polarization. The wave is linear polarized in regions from the outer magnetosphere (right side of plot) to the turning point. Earthward of the turning point, the polarization becomes counterclockwise. There is a 180° phase shift across the resonance, from counterclockwise to clockwise, in an Earthward approach. The features of these computed

polarizations and phases are very similar to what we have observed in the MPA and magnetometer data. The region of counter clockwise polarization seen in the magnetometer data (Figures 4.10, 4.16 and 4.19) likely corresponds to the interval between the resonance and the approximate position of the turning point. These features are illustrated in the schematic in Figure 5.2.

5.2 The resonance seen in phase shift in the MPA aurora

In many experimental studies of field line resonances, the 180° latitudinal phase shift has been used to identify the region of the resonance (Walker et al., 1979). Walker et al., used the STARE radar to observe drifting plasma irregularities in the ionosphere E region of the day side magnetosphere. The drift velocities of these irregularities can be used to determine the electric fields of the resonance. In evaluating their data, they used the SCH pulsation model, with large k_y . Consequently, there is no turning point in their model, and they do not consider the second 180° phase shift, which should occur poleward of the resonance (see Figure 2.6).

In our tunnel coupling model, we consider the full solution for the wave fields, including the turning point and consequently the azimuthal wave number k_y plays an important role in determining coupling to the resonance. We can use our numerical solutions to compute the phases for the compressional component B_{1z} and field line displacements ξ_x and ξ_y . These phases are plotted in Figure 2.6. In the high latitude from the magnetopause toward the turning point, the phases of all three components decrease with decreasing latitude, but the phase of the component ξ_x has a local minimum at the turning point. The component ξ_y has two latitudinal phase changes of 180° , a sharp phase change at the resonance, and the other, due to wave reflection, a gradual change between the turning point and the outer magnetosphere. Consequently there is V-shaped structure in the

latitude phase plots which is very similar to that seen in the phases in the MPA data (see Figures 4.13, 4.14 and 4.22; and the schematic in Figure 5.2).

5.3 Modulated optical arcs and inverted V

In this section, we hope to establish the relation between auroral arcs modulated by Alfvén resonance and the so called inverted V potential structures (Arnoldy, 1981). Both inverted V's and the phase structures in the MPA data have similar spatial scale sizes. Inverted V's are typically a few hundred *km* in latitude width when detected aboard satellites (Arnoldy, 1981). The optical modulated arcs observed in our data are 1° to 3° in latitudinal width, about 100 to 300 *km*. Secondly, the inverted V events occur primarily in the evening sector auroral oval. Our theoretical model and observational data cover this region. Inverted V potential structures and the perpendicular electric field of shear Alfvén resonance have a similar topology (Nishida, 1978). Finally the energy of precipitating electrons in the modulated arcs increases toward the center of the arcs as would be expected from an inverted V potential structure (compare Figures 4.19 and 4.20).

In practice, if we wish to study the parallel electric fields in shear Alfvén waves which might lead to inverted potential structure, we have to consider kinetic effects in a two dimensional space. Even though our model is for a cold plasma environment and does not allow kinetic effects, it still has some features or scale sizes which are similar to those found in inverted V's. Our tunnel coupling model allows us to estimate the width of the resonant coupling region for typical magnetospheric parameters. If we select the resonant point at 69° Invariant latitude ($7.8 R_e$ on the equator), an Alfvén velocity of 400 *km/s*, and a frequency 1.3 *mHz*, then the radial distance between the resonance and turning point is about 2.7 R_e . This width mapped to the auroral zone is about 200 to 300 *km*, which is a typical scale size for inverted V's.

We can use (2.10) to obtain the perpendicular electric fields from ξ_x and ξ_y , giving $E_x \propto -iY_3$, and $E_y \propto iY_2$. The amplitude and phase of Y_2 and Y_3 are plotted in Figures 2.3 to 2.6. The largest component at the resonance has a 180° phase shift across the resonance. This picture matches the configuration of the perpendicular or north south fields seen in inverted V's.

5.4 Conclusions

The data and our interpretation based on the field line resonance lead us to the following conclusions:

(1) We have confirmed the fact that resonant Alfvén waves on field lines threading the auroral oval strongly modulate the precipitation of auroral electrons. The frequency of the modulated emissions is near 1.3 mHz , which is the frequency associated with oscillations on closed dipole-like field lines (Samson, 1991a). The position of the maximum power of the oscillations in the 5577 \AA emissions (and energetic electrons) corresponds to the zero crossing of the ellipticity of the magnetic fields as well as the latitudinal maximum in the power of the oscillations in the magnetic fields.

(2) We have established a tunnel coupling model and find that the modulation of the electron precipitation occurs over the whole region between the turning point and the resonance. This region is determined by the region of positive ellipticity in the magnetometer data (Figure 5.2). The modulated 6300 \AA emissions have two 180° latitudinal phase shifts in support of the tunnel coupling model.

(3) There is a further suggestion from the comparison in the observational evidence and macroscopic model that resonant Alfvén waves might be associated with the inverted V's electric fields that cause arcs to form.

We think that the work presented in this thesis gives sufficient information

to begin the construction of a model connecting auroral particle precipitation with field line resonances, though much remains to be done. We have not yet developed a complete picture of the mode conversion to the kinetic Alfvén waves, the formation of field-aligned electric fields and the energization of electrons. We also need further optical measurements, with much better spatial resolution so as to determine whether the kinetic Alfvén waves might be an important component of shear Alfvén resonances.

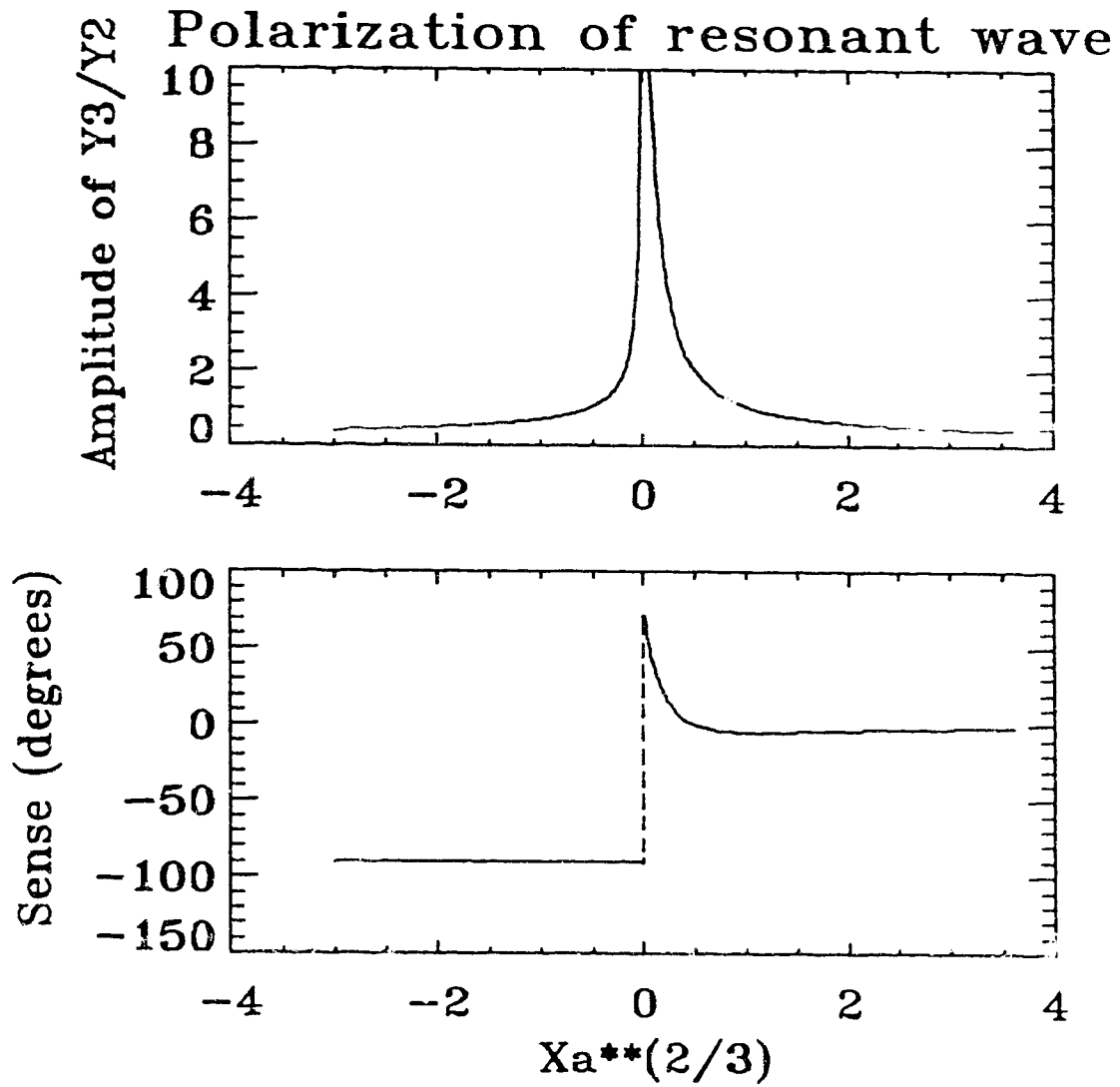


Figure 5.1: The polarization ratio ξ_x/ξ_y . Y_2 and Y_3 are normalized ξ_x and ξ_y defined in Chapter 2.

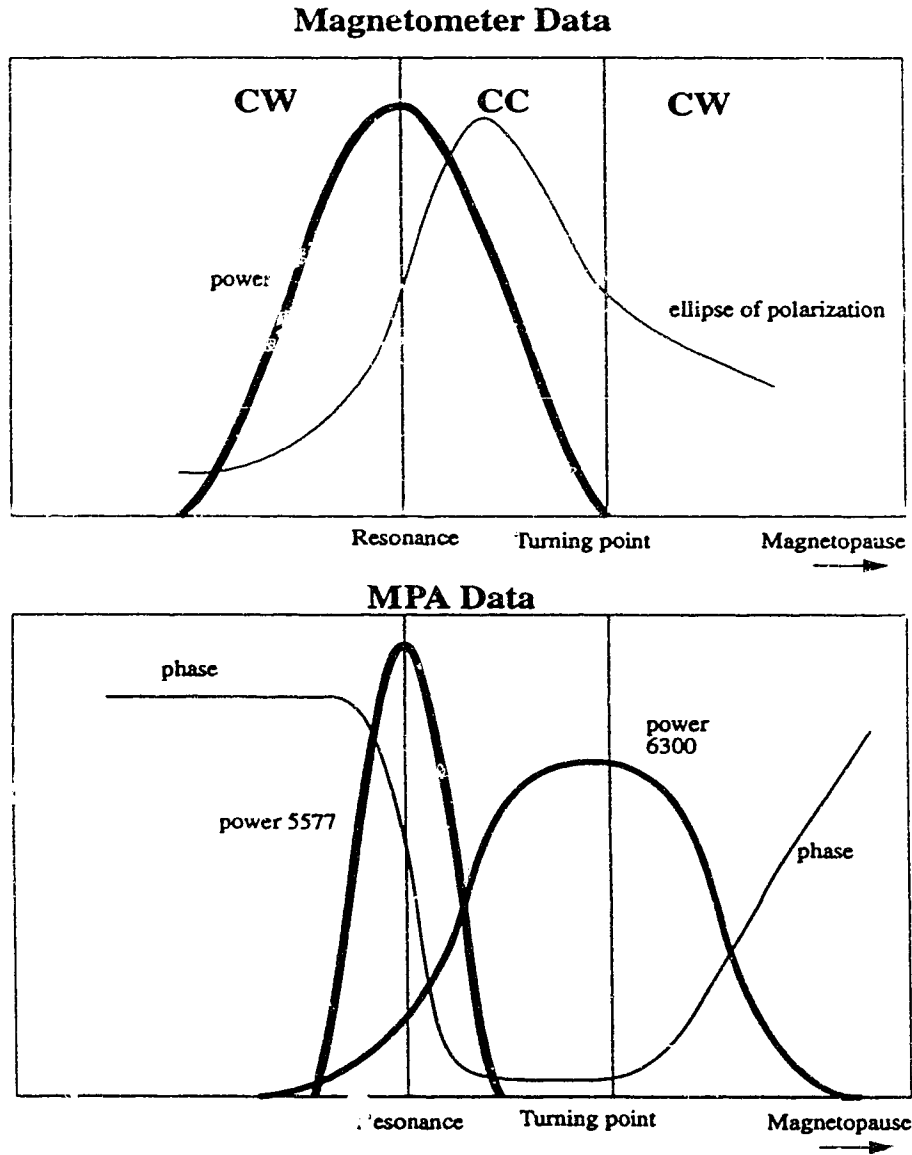


Figure 5.2: Top: (a) Schematic representation for resonant magnetometer data. CW means clockwise polarization, and CC is counterclockwise polarization. Bottom: (b) Schematic representation for modulated MPA data.

APPENDIX A

BUDDEN'S COMPUTATIONAL METHOD

Budden's method is to make an isosceles triangle on both anti Stokes lines, at $\arg \zeta = \frac{\pi}{3}$ and $\arg \zeta = \pi$, then to integrate from P point along the line r to point Q. On the integral path, there is a relation between ζ and the variable r (see the figure in this appendix). Specifically

$$\zeta_q - \zeta_p = d(e^{i\pi} - e^{i\frac{\pi}{3}}) = -d \cos(\frac{\pi}{6})e^{i\frac{\pi}{6}}$$

so that

$$d\zeta = -dr e^{i\frac{\pi}{6}} . \tag{A.1}$$

The ordinary differential equation becomes

$$\frac{dY_1}{dr} = -\zeta e^{i\frac{\pi}{6}} Y_2 \tag{A.2}$$

$$\frac{dY_2}{dr} = -\frac{\zeta + q}{\zeta} e^{i\frac{\pi}{6}} Y_1 . \tag{A.3}$$

In this set of equations, the integral variable r is a real number although the equations are complex, so it is not necessary to separate the equation into real and imaginary parts. We can integrate the complex equations directly. At point P, we have the initial conditions

$$Y_2 = 1 . \tag{A.4}$$

$$k = e^{i\frac{\pi}{12}} d^{\frac{1}{4}} \exp[-\frac{2}{3}(e^{i\frac{\pi}{3}} d + q)^{\frac{3}{2}}] . \tag{A.5}$$

$$Y_1 = -\left\{ \frac{1}{4(\zeta + q)} + \frac{\zeta}{(\zeta + q)^{\frac{1}{2}}} \right\} Y_2 . \tag{A.6}$$

With these starting values, the set of equations are integrated from point P toward Q. At point Q the numerical result should match the asymptotic solution of equation (2.56) . Then \Re can be determined by using different values of q. The method avoids the singular point on the real axis of the complex plane.

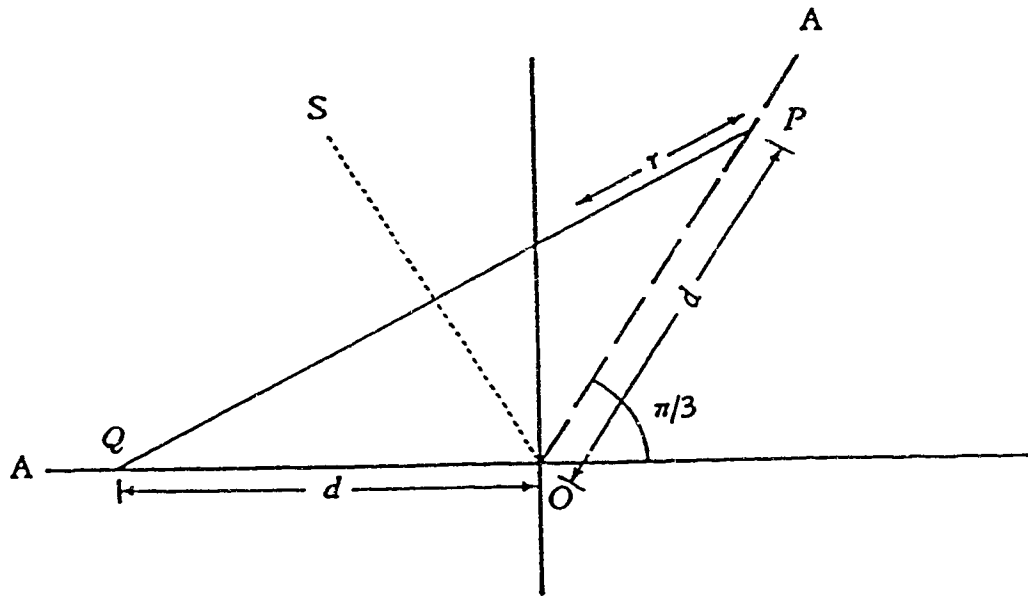


Figure A.1: ζ complex plane, the Stokes lines are at $\arg\zeta = 0$ and $\arg\zeta = \frac{2\pi}{3}$, and the Anti Stokes lines are at $\arg\zeta = \frac{\pi}{3}$ and $\arg\zeta = \pi$ (after Budden, 1961).

APPENDIX B

COMPLEX DEMODULATION METHOD

The process of complex demodulation as applied to time series $x(t)$ is defined in terms of two very simple mathematical operations. First, each frequency band of interest in the spectrum is shifted to zero frequency by multiplying each term of the time series by the complex exponential function $\exp(-i\omega't)$. ω' is the central frequency of the shifted band. A new series $X_s(\omega', t)$ is produced for each frequency band, i.e.

$$X_s(\omega', t) = x(t) \exp(-i\omega't). \quad (\text{B.1})$$

Secondly, the new frequency-shifted series is low-pass filtered using a set of weights $a_k (k = -m, \dots, m)$, and the result is the complex demodulated time series $X_d(\omega', t)$

$$X_d(\omega', t) = \sum_{k=-m}^{k=+m} a_k X_s(\omega', t + k\Delta t). \quad (\text{B.2})$$

Alternatively, this demodulated time-series may be expressed in terms of its modulus and phase as

$$X_d(\omega', t) = |X_d(\omega', t)| \exp[-i\phi(\omega', t)]. \quad (\text{B.3})$$

Let us suppose that the data contain a periodic component that would produce a peak in the spectrum at frequency ω_0

$$x(t) = A \cos(\omega_0 t + \gamma), \quad (\text{B.4})$$

producing the frequency-shifted demodulation

$$X_s(\omega', t) = \frac{A}{2} \left\{ \exp[-i(\delta\omega t - \gamma)] + \exp[-i(2\omega_0 + \delta\omega)t + \gamma] \right\}. \quad (\text{B.5})$$

$X_s(\omega', t)$ is centred on the frequency $\omega' = \omega_0 + \delta\omega$ and therefore contains components at frequencies $-\delta\omega$ and $-(2\omega_0 + \delta\omega)$.

The frequency-shifted series is low-pass filtered, and remaining the component at $-(2\omega_0 + \delta\omega)$, giving

$$X_d(\omega_0 + \delta\omega, t) = \frac{A}{2} \exp[-i(\delta\omega t - \gamma)]. \quad (\text{B.6})$$

The phase, ϕ_d , is therefore,

$$\phi_d = -\delta\omega t + \gamma. \quad (\text{B.7})$$

We get the first data point of the demodulated series at $t = 0$, i.e.

$$X_d(\omega_0 + \delta\omega) = \frac{A}{2} \exp(i\gamma). \quad (\text{B.8})$$

The expression includes the periodic frequency ω_0 and its bias $\delta\omega$. If we know the periodic frequency ω_0 from the FFT analysis, we can immediately obtain its phase from above equation. A schematic diagram of the procedure for computing complex demodulation is given in Figure B.1.

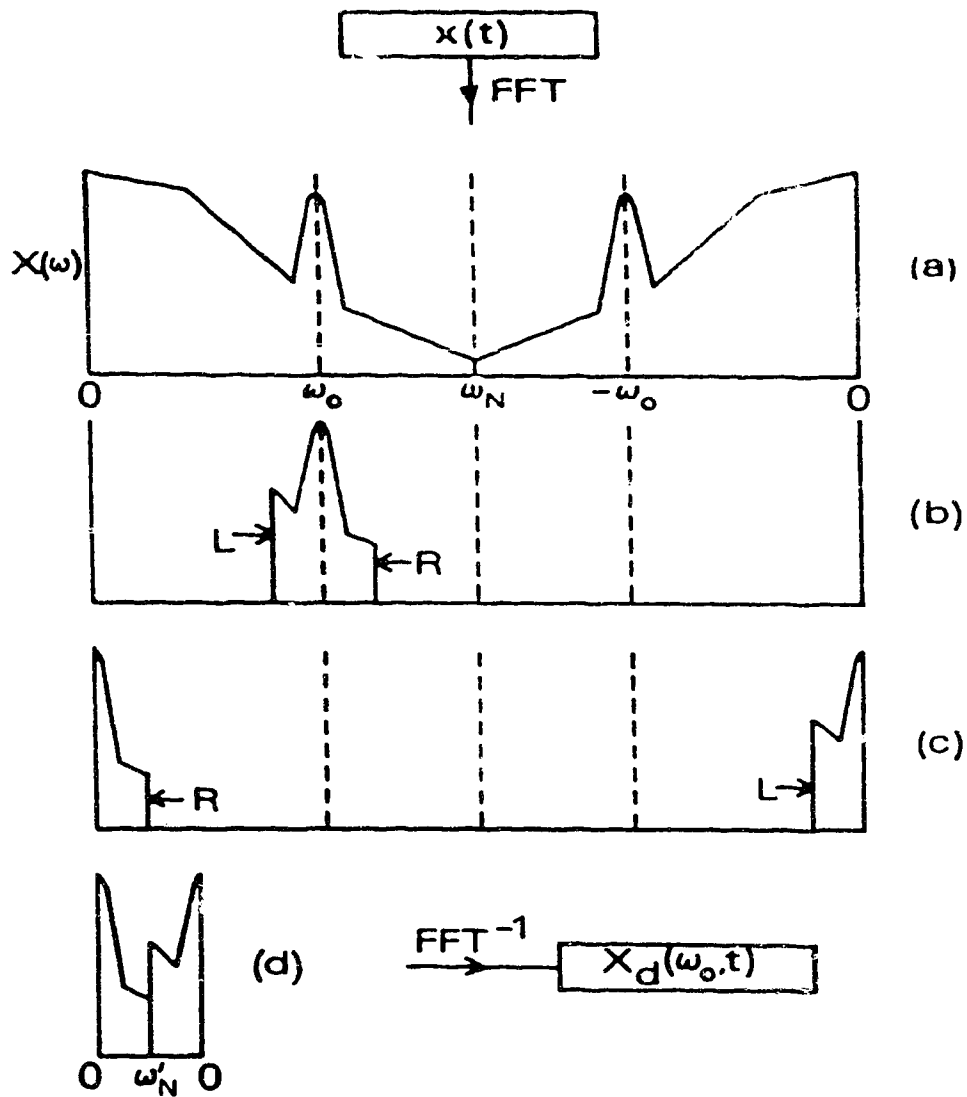


Figure B.1: Schematic diagram of the procedure for computing the complex demodulation $X_d(\omega_0, t)$ from the time series $x(t)$. (a) Raw Fourier spectrum; (b) Filtered spectrum; (c) Frequency shifted spectrum; (d) Truncated frequency shifted spectrum (after Banks, 1975).

BIBLIOGRAPHY

- Akasofu, S.-I., Auroral arcs and auroral potential structure, in *Physics of Auroral Arc Formation*, Geophysical Monograph 25, ed. by S.-I. Akasofu and J. F. Kan, American Geophysical Union, Washington DC, 1, 1981.
- Allan, W., White, S. P. and Poulter, E. M., Impulse-excited hydromagnetic cavity and field-line resonances in the magnetosphere, *Planet. Space Sci.*, 34, 371, 1986.
- Arnoldy, R. L., Review of auroral particle precipitation, in *Physics of auroral arc formation*, Geophysical Monograph 25, ed. by S.-I. Akasofu and J. F. Kan, American Geophysical Union, Washington DC, 56, 1981.
- Banks, R. J., Complex demodulation of geomagnetic data and the estimation of transfer functions, *Geophys. J. R. astr. Soc.*, 43, 87, 1975.
- Beamish, D., Complex demodulation applied to Pi2 geomagnetic pulsations, *Geophys. J. R. astr. Soc.*, 58, 471, 1979.
- Berkey, F. T., V. M. Driatsky et al, A synoptic investigation of particle precipitation dynamics for 60 substorms in IQSY (1964-65) and IASY (1969), *Planet. Space Sci.*, 22, 255, 1974.
- Budden, K. G., Radio waves in the ionosphere, Cambridge U. Press, London, 1961.
- Campbell, W. W. and Rees, M. H., A study of auroral coruscations, *J. Geophys. Res.*, 66, 41, 1961.
- Chen, L. and Hasegawa, A., Plasma heating by spatial resonance of Alfvén wave, *Physics of Fluids*, 17, 7, 1974.
- Chen, L. and Hasegawa, A., A theory of long-period magnetic pulsations, 1, steady state excitation of field line resonance, *J. Geophys. Res.*, 79, 1024,

- 1974a.
- Chen, L. and Hasegawa, A., A theory of long-period magnetic pulsations. 2. Impulse excitation of surface eigenmode, *J. Geophys. Res.*, **79**, 1033, 1974b.
- Cole, K. D., Eccentric Dipole Coordinates, *Aust. J. Phys.*, **16**, 423, 1963.
- Denisov, N. G., On a singularity of the field of an electromagnetic wave propagated in an inhomogeneous plasma, *Soviet Physics JETP*, Vol. 4, No. 4, 544, 1957.
- Dungey, R. L., Electrodynamics of the outer atmosphere, *Penn. State Ionos. Res. Lab Sci.* **14**, 1273, 1954.
- Fukunishi, H., Dynamic relationship between proton and electron auroral substorms, *J. Geophys. Res.*, **80**, 553, 1975.
- Galperin, Yu. I. and Ya. I. Feldstein, Auroral luminosity and its relationship to magnetospheric plasma domains, in *Auroral Physics*, ed. by C.-I. Meng, M.J. Ryeroff, L.A. Frank, Cambridge Univ. Press, England, 207, 1990.
- Goertz, C. K., Magnetosphere-ionosphere coupling, *J. Geophys. Res.*, **84**, 7239, 1979.
- Goertz, C. K., Discrete breakup arcs and kinetic Alfvén waves, in *Physics of Auroral Arc Formation* Geophysical Monograph 25, ed. by S.-I. Akasofu and J. F. Kan, American Geophysical Union, Washington DC 451, 1981.
- Goertz, C. K., Kinetic Alfvén wave on auroral field lines, *Planet. Space Sci.*, **32**, 1387, 1984.
- Greenwald, R. A. and Walker, A. D. M., Energetics of long period resonant hydromagnetic waves, *Geophys. R. Lett.*, **77**, 749, 1980.
- Hasegawa, A. and Chen, L. Kinetic process of plasma heating due to Alfvén wave excitation, *Phys. Rev. Lett.*, **35**, 370, 1975.

- Hasegawa, A., Particle acceleration by MHD surface wave and formation of aurora, *J. Geophys. Res.* , 81, 5083, 1976.
- Hasegawa, A. and Mima, K., Anomalous transport produced by kinetic Alfvén wave turbulence, *J. Geophys. Res.* , 83, 1117, 1978.
- Hasegawa, A. and Maclellan, C. G., Field-aligned electric field accompanied by drift Alfvén waves in an inhomogeneous plasma, *Geophys. Res. Lett.* , 17, 1605, 1990.
- Hirsch, P., Transient E-mode propagation in a plane-stratified plasma, *Radio Sci.*, 2, 4, 1967.
- Hughes, W. J., The screening of micropulsation signals by the atmosphere and ionosphere, *J. Geophys. Res.*, 81, 3234, 1976.
- International Association of Geomagnetism and Aeronomy, *International Auroral Atlas* , IAGA publication No. 18, University Press Edinburgh, 1963.
- Kivelson, M. G. and Southwood, D. J., Resonant ULF waves: A new interpretation, *Geophys. Res. Lett.* , 12, 49, 1985.
- Kivelson, M. G., Coupling of global magnetospheric MHD eigenmodes to field line resonances, *J. Geophys. Res.* , 91, 4, 1986.
- Lam, H. L. and G. Rostoker, The relationship of Pc5 micropulsation activity in the morning sector to auroral westward electrojet, *Planet. Space Sci.*, 26, 473, 1978.
- Newell, P. T., Identification and observations of the plasma mantle at low altitude, *J. Geophys. Res.* , 96, 35, 1991.
- Nishida, A., Geomagnetic diagnosis of the magnetosphere, *Physics and Chemistry in Space* 9, Springer-Verlag, p147, 1978.

- Olson, J. V., G. Rostoker and G. Olchowy, A study of concurrent riometer and magnetometer variations in the Pc4-5 pulsation band, *J. Geophys. Res.*, 85, 1695, 1980.
- Omholt, A., *The Optical Auroral*, Springer-Verlag, Press, 1971.
- Ott, E., Theory of plasma heating by magnetosonic cavity mode absorption, *Phys. Fluids*, 21, 12, 1978.
- Piliya, A. D., Wave conversion in an inhomogeneous plasma, *Soviet Physics – Technical Physics*, 11, 5, 1966.
- Rees, M. H. and Benedict, P. C., Proton auroral oval, *J. Geophys. Res.*, 75, 4763, 1970.
- Rees, M. H. and Luckey, D., Auroral electron energy derived from ratio of spectroscopic emissions I. Model computations, *J. Geophys. Res.*, 79, 5181, 1974.
- Roberts, B., Waves in inhomogeneous media, *Proceedings of the European Meeting on Solar Physics*, 1984.
- Romick, G. J. and Belon, A. E., The spatial variation of auroral luminosity-1, The behavior of synthetic model auroras, *Planet. Space Sci.*, 15, 475, 1966.
- Romick, G. J. and Belon, A. E., The spatial variation of auroral luminosity-2, determination of volume emission rate profiles, *Planet. Space Sci.*, 15, 1695, 1967.
- Rostoker, G., Magnetospheric substorms definition and signatures, *J. Geophys. Res.*, 85, 1663, 1980.
- Saito, T., Geomagnetic pulsations, *Space Sci. Rev.*, 10, 319, 1969.
- Samson J. C., Three-dimensional polarization characteristics of high-latitude Pc5 geomagnetic micropulsations, *J. Geophys. Res.*, 77, 6145, 1972.

- Samson, J. C., Pure states, polarized waves, and principal components in the spectra of multiple geophysical time series, *Geophys. J. R. astr. Soc.* , 72, 647, 1983.
- Samson, J. C., Geomagnetism Vol. 4, ed. by J. A. Jacob, Chapter 4, 481, 1991.
- Samson, J. C., T. J. Hughes, Observations of a detached, discrete arc in association with field line resonances, submitted to the *J. Geophys. Res.* , 1991a
- Samson, J. C., R. A. Greenwald, Magnetometer and radar observations of MHD cavity modes in the earth's magnetosphere, *Can. J. of Phys.*, in press, 1991b.
- Samson, J. C., D. D. Wallis, Substorm intensification and field line resonances in the nightside magnetosphere, submitted to the *J. Geophys. Res.*, 1991c.
- Southwood, D. J., Some features of field line resonance in the magnetosphere, *Planet. Space Sci.* , 22, 483, 1974.
- Speziale, T., Linear wave conversion in an unmagnetized, collisionless plasma, *The Physics of Fluids*, 20, 6, 1977.
- Stix, T. H., *The Theory of Plasma Waves*, McGraw-Hill, p242, 1962.
- Tamao, T., Transmission and coupling resonance of hydromagnetic disturbances in the non-uniform earth's magnetosphere, *Sci. Rep. Tohoku Univ., Ser.* 5, 17, 43, 1966.
- Vallance Jones, A., F. Creutzberg, R. L. Gattinger and F. R. Harris, Auroral studies with a chain of meridian-scanning photometers. 1. Observations of proton and electron aurora in magnetospheric substorms, *J. Geophys. Res.*, 80, 553, 1982.
- Walker, A. D. M. and Greenwald, R. A., State auroral radar observations of Pc5 geomagnetic pulsations, *J. Geophys. Res.* , 84, 3373, 1979.

- Walker, A. D. M. and Greenwald, R. A., Pulsation structure in the ionosphere derived from auroral radar data, in *ULF Pulsations in the Magnetosphere*, ed. by D. J. Southwood, Center for academic publications Japan, Tokyo, 111, 1981.
- Wiens, R. H. and Vallance Jones *et al.*, Studies of auroral hydrogen emissions in west-central Canada. 3. Proton and electron auroral ovals, *Can. J. of Phys.*, 47, 1493, 1969.
- Zhu, X. M. and Kivelson, M. G., Analytic formulation and quantitative solutions of the coupled ULF wave problem, *J. Geophys. Res.*, 93, 8602, 1988.